J. Fluid Mech. (1998), *vol.* 360, *pp.* 295–340. Printed in the United Kingdom

Statistical modelling and direct numerical simulations of decaying stably stratified turbulence. Part 1. Flow energetics

By C. STAQUET[1]† AND F. S. GODEFERD[2]

[1] Laboratoire de Physique, Ecole Normale Supérieure de Lyon, 46 allée d'Italie, 69364 Lyon cedex 07, France

[2] Laboratoire de Mécanique des Fluides et d'Acoustique UMR n° 5509, Ecole Centrale de Lyon BP 163, 69131 Ecully cedex, France

(Received 11 February 1997 and in revised form 27 November 1997)

The dynamics of a homogeneous turbulent flow subjected to a stable stratification are studied by means of direct numerical simulations (DNS) and by a two-point closure statistical EDQNM model, adapted for anisotropic flows by Cambon (1989). The purpose of this work is to investigate the validity of the anisotropic statistical model, which we refer to as the $EDQNM_2$ model. The numerical simulations are of high resolution, 256^3, which permits Reynolds numbers comparable to those of recent laboratory experiments. Thus, detailed comparisons with the wind-tunnel experiments of Lienhardt & Van Atta (1990) and Yoon & Warhaft (1990) are also presented.

The initial condition is chosen so as to test the anisotropic closure assumption of the $EDQNM_2$ model. This choice yields a ratio of kinetic to potential energy of 2 : 1. This important amount of initial potential energy drives the flow dynamics during the first Brunt–Väisälä period. Because stronger transfer rates of potential energy than of kinetic energy occur toward small scales, the heat flux is (persistently) counter gradient at those small scales. The loss of potential energy at large scales is partly made up for by conversion of vertical kinetic energy, and this sets up a down-gradient heat flux at those scales, as if no or little potential energy were present at the initial time. Thus, common features with wind-tunnel experiments (in which there is relatively little potential energy just behind the grid) are found. Interestingly, only one quantity displays a similarity law in the DNS, in the $EDQNM_2$ model and in the experiments of Lienhardt & Van Atta (1990) and Yoon & Warhaft (1990) as well: this is the ratio of the vertical heat flux to the dissipation rate of kinetic energy, which can also be interpreted as an instantaneous mixing efficiency. Thus, this parameter seems to be independent of initial flow conditions.

Our calculations simulate a longer evolution of the flow dynamics than laboratory experiments (in which the flow develops for at most one Brunt–Väisälä period). We find that the flow dynamics change from about 1.5 Brunt–Väisälä periods. At that time, the heat flux collapses while the dissipation rate of kinetic energy displays a self-similarity law attesting that this quantity becomes driven by buoyancy forces. This permits us to link the collapse of the largest scales of the flow with the smallest scales being influenced by the buoyancy force. We finally discuss the influence of a geometrical confinement effect upon the above results.

The $EDQNM_2$ model compares remarkably well with the DNS, with respect to previous statistical models of stably stratified turbulent flows. Insufficient decorrelation between the vertical velocity and the temperature fluctuations is however

† Present address: LEGI, BP53, 38041 Grenoble cedex 9, France.

observed, but with no dynamical significance. The vortex part of the flow is also overestimated by the $EDQNM_2$ model, but the relative difference between the model prediction and the DNS does not exceed 15 % after 6 Brunt–Väisälä periods. The $EDQNM_2$ model offers interesting perpectives because of its ability to predict the dynamics of stratified flows at high Reynolds numbers. Knowledge about small-scale behaviour will be especially useful, to build up parameterization of the subgrid scales for instance.

1. Introduction

Flows subjected to a stable buoyancy force display a ubiquitous nature. Most of the oceanic water mass, except for the mixed layer below the surface, is stably stratified. In the upper atmosphere, the small-scale dynamics of the stratosphere are dominated by internal waves that locally break (Sidi 1995). For stellar interiors, Schatzman (1993, 1996) has proposed that a random field of linear internal waves may exist below the convective envelope of the Sun, that would transport chemical species, such a lithium, to the core of the star. This mechanism would account for lithium depletion measured in the Sun, compared to the primitive abundance of this species. Stably stratified regions are also found in cooling circuits of nuclear reactors and the reduction of turbulent diffusion may yield very strong local temperature gradients that damage the boundaries of the circuits.

In this paper, we shall restrict our study to homogeneous turbulent flows, subjected to a stable temperature profile varying linearly with height. The fluid is therefore uniformly stratified. We shall ignore the influence of any external shear, rotation or forcing. Our purpose is to validate a two-point closure anisotropic statistical model of the EDQNM type (eddy damped quasi-normal Markovian) for homogeneous axisymmetric stably stratified turbulence. Validation is performed against high resolution (256^3) direct numerical simulations (DNS). The EDQNM model was developed for homogeneous isotropic turbulence by several authors, its final form being due to Orszag (1970, 1977) (see Lesieur 1990 for a review). It has been successfully validated (e.g. André & Lesieur 1977). The EDQNM model discussed in the present paper is an adaptation by Cambon (Cambon 1989) of the original isotropic model to account for the anisotropic influence of a buoyancy force on a turbulent homogeneous flow. This anisotropic model will be referred to as the $EDQNM_2$ model hereafter.

Attempts have been made in the past to extend to stably stratified turbulence statistical models originally developed for homogeneous isotropic turbulence. Thus, the anisotropic influence of internal waves was introduced in an EDQNM model by two research groups, in two spatial dimensions in a vertical plane (Holloway & Hendershot 1977; Holloway 1979; Carnevale & Frederiksen 1983). In the model of Holloway & Hendershot, the anisotropy was taken into account in the closure model only, the spectra depending upon the wavevector magnitude (and upon time). The EDQNM predictions were compared to results of two-dimensional direct numerical simulations (Holloway & Ramsden 1988) and a rough qualitative agreement was found. In Carnevale & Frederiksen's model, severe simplifications were used that led to spurious conservation laws (see Holloway 1988, for a full discussion). In three dimensions, direct interaction approximation theory was applied to stably stratified turbulence but the complexity of the theory made it of practical use only once

severely simplified (Sanderson, Hill & Herring 1986; Sanderson *et al.* 1991). One advantage of the $EDQNM_2$ model used in the present paper is its tractability, though anisotropy is taken into account both in the closure assumption and in the energy spectra: all quantities depend upon the wavevector magnitude and upon its angle with respect to the vertical. Another approach entirely has been followed recently by Daubner & Zeitlin (1996), using the formalism of weak interaction theory. This formalism, normally dealing with Lagrangian variables, was developed and successfully applied in the past to a variety of waves but not to internal gravity waves (see Zakharov, L'vov & Falkovich 1992, for a review). For comparison purposes with *in situ* and laboratory measurements, Daubner & Zeitlin (1996) derived stationary spectra in Eulerian coordinates for internal gravity waves in a two-dimensional vertical plane.

Predictions of the linearized Boussinesq equations have also been investigated. This approximation coincides with the rapid distortion theory (RDT). The interest in this linear approach is that the flow dynamics can be predicted exactly from initial conditions through analytical expressions (possibly requiring numerical resolution, but at a weak computational cost). As shown by Hanazaki & Hunt (1996), a remarkably good agreement between RDT and numerical or experimental results can be obtained in situations where the heat flux is strong. This is the case when no or little potential energy is present at the initial time, as in grid turbulence experiments and in previous numerical experiments, which we discuss now.

Several laboratory experiments on homogeneous unsheared stably stratified turbulence have been performed. Earlier experiments dealt with salt water, either in a tow tank (e.g. Spedding, Browand & Fincham 1996, for the most recent experiment of this type) or in a channel with uniform mean flow (Itsweire, Helland & Van Atta 1986 and references therein). Wind-tunnel experiments on homogeneous grid-generated turbulence have been performed more recently, by Lienhardt & Van Atta (1990), Yoon & Warhaft (1990), Thoroddsen & Van Atta (1992, 1996) and Komori & Nagata (1996) for instance. The Prandtl number of our numerical simulations, equal to 1, is comparable to that of these experiments (for room temperature, in air, $Pr = 0.7$) so that comparison, when possible, will be made with the latter works. Thoroddsen & Van Atta (1992, 1996) mainly report on the anisotropy of the flow, while Komori & Nagata (1996) present a detailed investigation of the influence of the Prandtl number upon counter-gradient events. Thus, we shall rather compare our numerical results with the data of Lienhardt & Van Atta (1990, referred to herein as LVA) and Yoon & Warhaft (1990, referred to herein YW), where a detailed investigation of the overall flow dynamics is presented.

Though the experimental conditions of these two wind-tunnel experiments are close, very different dynamics are found. As analysed by YW, these differences may be due to the higher values of the Brunt–Väisälä frequency used in LVA's experiments, which lead to a quicker build-up of potential energy behind the grid. Thus, in LVA's experiments, a two-scale behaviour is found, buoyancy forces dominating at large scales and dissipation at small scales. This two-scale behaviour yields remarkable universal scaling laws, distinct for large and small scales. In YW's work by contrast, three different stages can be successively distinguished depending upon a turbulent Richardson number, stratification effects progressively modifying the small-scale behaviour. Data are found to better collapse when plotted against this parameter. For their most stable experiment, YW even observed a significant net counter-gradient heat flux. It should be pointed out that both experiments were conducted over a rather short time relative to the characteristic period of the waves, of only one

period, because the thermal expansion coefficient of air, that relates temperature and density fluctuations, is small. No internal waves were detected in either work during turbulence decay, unlike salt water experiments.

Several three-dimensional numerical studies of decaying stratified homogeneous turbulence have already been performed, within the Boussinesq approximation. These studies mainly differ by the initial conditions. In Riley, Metcalfe & Weissman (1981), Métais & Herring (1989) or Gerz & Schumann (1991), the initial condition is designed as a model of the flow just behind the grid in laboratory experiments; thus, a homogeneous and isotropic turbulent flow with no potential energy is used to initiate the calculations. The resolution is 32^3 in the work of Riley *et al.* and 64^3 in the other studies. In these works, a so-called 'collapse' of turbulence is found, that affects both the dynamical properties of the flow (e.g. reduction of energy transfers), and its structure (inhibition of vertical scales growth). The influence of a forcing was examined in Herring & Métais (1989) and in Ramsden & Holloway (1992). In Métais & Lesieur (1992), large-eddy simulations are compared to 128^3 DNS for isotropic and stably stratified turbulence. The second group of simulations is complementary to the first: the evolution of a stratified flow initiated by a reservoir of potential energy only is addressed. In Chasnov (1996), similarity states at high Reynolds number were derived and tested against large-eddy simulations. In Gerz & Yamazaki (1993), results of 64^3 and 128^3 DNS are presented and analysed from the point of view of oceanic turbulence. Lagrangian properties of stably stratified turbulence have been recently studied by Kimura & Herring (1996), using 128^3 DNS.

In the present paper, another initial condition is used, in which both initial kinetic and potential energies are non-zero, in a ratio 2 : 1. As detailed in § 4 below, this choice stems from the comparison with the EDQNM_2 model: it yields a flow dynamics nearly driven by the nonlinear terms of the equations, which therefore are most sensitive to the closure assumption (which relates triple correlations of the fields to double ones). This initial condition also yields a flow dynamics dominated by the internal wave part and this is again a severe situation for testing the EDQNM_2 model, which was originally designed for isotropic turbulent flows. The calculations are conducted over a much longer time than laboratory experiments, of 6 Brunt–Väisälä periods.

A simplified version of this EDQNM_2 model has already been tested against low-resolution (64^3) DNS (van Haren, Staquet & Cambon 1996). This simplified model will be referred to as the EDQNM_1 model hereafter. The simplification consists in dropping the contribution of the stable stratification in the closure assumption for the triple correlations, while retaining the influence of stable stratification on the flow dynamics through the linear terms in the equations. Hence, the closure assumption is formally identical to that used in the classical EDQNM model for isotropic turbulence. A rather good agreement between theory and DNS was still found, despite the fact that energy transfers toward small scales were too large in the EDQNM_1 model, because of this simplification. In the present paper, the predictions of the full model are tested against DNS, using the initial condition mentioned above.

Finally, note that our study is very different from the recent one by Herr, Wang & Collins (1996) who examine the behaviour of a *passive* scalar with uniform mean gradient by comparing direct numerical simulations and an EDQNM model. In that case, the flow field remains isotropic for all time. No scalar feedback on the velocity nor internal wave effects are present in the flow. Thus, in that EDQNM model, the closure can be operated independently in the equations for the kinetic energy spectrum and for the scalar variance spectrum.

In the next section, the equations of motions are detailed in physical and Fourier

space. The $EDQNM_2$ model is described in § 3, the detailed form of the transfer terms in this model and in the simplified $EDQNM_1$ version being given in the Appendix (more details can be found in Cambon 1989; van Haren 1993 and Godeferd & Cambon 1994). The numerical method used in the DNS is described in § 4, along with the initial conditions and the physical parameters of the flow. In the present paper, comparison between the $EDQNM_2$ model and DNS focuses on the temporal and spectral behaviour of the energy of the flow and of its components (§ 5). Comparison with the experimental works of LVA (1990) and YW (1990) are also presented.

Our main results are as follows. The early stage of the flow dynamics, for times smaller than $\simeq$ 1.5 Brunt–Väisälä periods, is controlled by the amount of initial potential energy. Kinetic and potential energy are transferred toward small scales, at a higher rate for the latter quantity. Thus, the total energy (kinetic+potential) decays at a higher rate than its isotropic counterpart. The loss of potential energy at large scales due to nonlinear transfers toward small scales is partly made up for by conversion of vertical kinetic energy, as if no or little potential energy were present at the initial time. Thus, common features with wind-tunnel experiments (in which there is relatively little potential energy just behind the grid) are found. At small scales, the excess of potential energy (relative to the initial equipartition in the 'wave' part of the flow) drives a counter-gradient heat flux, which persists all along the flow evolution. This counter-gradient flux exists despite the low value of the Prandtl number of our calculations (= 1) and is driven by our initial condition. However, we show that the small scales of the flow are still not dominated by buoyancy during this first stage.

From about $\simeq$ 1.5 Brunt–Väisälä periods, the large scales of the flow collapse and all scales of motions, up to the smallest, become controlled by buoyancy effects. As a consequence, clear similarity laws, for different values of the Brunt–Väisälä frequency and the viscosity, can be inferred from the data, for the vertical kinetic energy and for the dissipation rate of kinetic energy.

A very good agreement with the $EDQNM_2$ model is found in general. Two exceptions are the vortex part of the flow, made up of quasi-two-dimensional motions that emerge from turbulence from $\simeq$ 1.5 Brunt–Väisälä periods, and an insufficient decorrelation between the vertical velocity component and the temperature fluctuation. These discrepancies are however weak enough to be of no dynamical significance.

A detailed study of the anisotropic behaviour of the flow, at large and small scales, and of its mixing properties will be presented in a subsequent paper (Godeferd & Staquet 1998).

2. Equations of stably stratified homogeneous turbulence

2.1. *Basic equations*

Let (x, y, z) be a Cartesian coordinate system in a Galilean frame of reference, z being directed vertically upwards. The Boussinesq equations for a homogeneous stably stratified non-rotating flow are

$$\left(\frac{\partial}{\partial t} + u_j \frac{\partial}{\partial x_j} - \nu\nabla^2\right) u_i + \frac{\partial p}{\partial x_i} = T\delta_{i3}, \tag{1a}$$

$$\left(\frac{\partial}{\partial t} + u_j \frac{\partial}{\partial x_j} - \kappa\nabla^2\right) T = -N^2 u_3, \tag{1b}$$

$$\frac{\partial u_i}{\partial x_i} = 0. \tag{1c}$$

The components of the velocity field will be denoted (u_1, u_2, u_3) throughout the paper. $T(\boldsymbol{x}, t)$ denotes the temperature fluctuations about a background temperature $T_0 + T_b(z)$ of an hydrostatic stationary reference state. Note that $T(\boldsymbol{x}, t)$ has been rescaled as an acceleration, using the factor βg ($\beta g T$ is the dimensional temperature); β is the thermal expansion coefficient and g is the acceleration due to gravity. Equation (1 *c*) represents the mass conservation and, in the Boussinesq approximation, amounts to assuming that the flow is incompressible. The temperature diffusivity κ is taken equal to the kinematic viscosity ν in the temperature equation; thus the Prandtl number is equal to 1. In addition to ν and κ, a third physical parameter comes into play in the equations, N, that couples the velocity and temperature fields. N is the Brunt–Väisälä frequency:

$$N = \left(\beta g \frac{T_b}{dz}\right)^{1/2}. \tag{2}$$

The Brunt–Väisälä period $2\pi/N$ will be denoted T_{BV}.

When nonlinear interactions are neglected in (1), the linear regime of internal waves is recovered. The eigenmodes of the resulting equations can be computed and three frequencies are obtained. Two of them verify the dispersion relation of internal waves, $\omega = \pm N \sin\theta$, and are associated with propagating internal waves, the wavevector of which makes an angle θ to the vertical; the third frequency is $\omega = 0$ and is associated with a vortex (or non-propagating) motion (see e.g. Muller *et al.* 1986, for a full discussion).

Making use of the homogeneity hypothesis, one can Fourier transform all quantities that depend on the spatial variable $\boldsymbol{x}$, and get the spectral (Fourier) space equations for the corresponding Fourier components: $\hat{\boldsymbol{u}}(\boldsymbol{k}, t)$ for the velocity $\boldsymbol{u}$, and $\hat{T}(\boldsymbol{k}, t)$ for the temperature T, $\boldsymbol{k}$ being the wavevector. The incompressibility of the flow expressed in Fourier space is $\boldsymbol{k} \cdot \hat{\boldsymbol{u}} = 0$, so that the velocity vector in Fourier space is orthogonal to the wavevector. Equations (1 *a*) and (1 *b*) become, in Fourier space,

$$\left.\begin{aligned} \left(\frac{\partial}{\partial t} + \nu k^2\right)\hat{u}_i(\boldsymbol{k}) - P_{i3}(\boldsymbol{k}, t)\hat{T}(\boldsymbol{k}, t) &= -\mathrm{i}\, k_l P_{in}(\boldsymbol{k}) \int_{\boldsymbol{k}+\boldsymbol{p}+\boldsymbol{q}=0} \hat{u}_n(\boldsymbol{p}, t)\hat{u}_l(\boldsymbol{q}, t)\, \mathrm{d}^3\boldsymbol{p}, \\ \left(\frac{\partial}{\partial t} + \nu k^2\right)\hat{T}(\boldsymbol{k}) + N^2\hat{u}_3(\boldsymbol{k}, t) &= -\mathrm{i}\, k_l \int_{\boldsymbol{k}+\boldsymbol{p}+\boldsymbol{q}=0} \hat{u}_l(\boldsymbol{p}, t)\hat{T}(\boldsymbol{q}, t)\, \mathrm{d}^3\boldsymbol{p}. \end{aligned}\right\} \tag{3}$$

$P_{ij} = \delta_{ij} - k_i k_j / k^2$ is the projection operator onto the plane orthogonal to $\hat{\boldsymbol{u}}(\boldsymbol{k})$, δ_{ij} denotes the Kronecker tensor and $\mathrm{i}^2 = -1$.

2.2. *Wave/vortex decomposition*

We use the following decomposition in Fourier space:

$$\hat{u}_i = \hat{\phi}^1 e_i^1 + \hat{\phi}^2 e_i^2, \tag{4}$$

where the unit vectors $\mathbf{e}^1$ and $\mathbf{e}^2$ are defined as follows. Since $\boldsymbol{u}$ is perpendicular to $\boldsymbol{k}$, a local frame of reference is defined in Fourier space, made up of the wavevector $\boldsymbol{k}$ and of two unit vectors lying in a plane, Π say, perpendicular to $\boldsymbol{k}$. One of these vectors, $\mathbf{e}^1(\boldsymbol{k})$, is taken horizontal so that the second vector, $\mathbf{e}^2(\boldsymbol{k})$, lies along the intersection of Π and a vertical plane. This frame is usually referred to as the Craya–Herring frame and was proposed by Craya (1958) and Herring (1974) for axisymmetric turbulence. The two unit vectors are defined by

$$\mathbf{e}^1(\boldsymbol{k}) = (\boldsymbol{k} \times \boldsymbol{n})/|\boldsymbol{k} \times \boldsymbol{n}|, \quad \mathbf{e}^2(\boldsymbol{k}) = (\boldsymbol{k} \times \mathbf{e}^1)/|\boldsymbol{k} \times \mathbf{e}^1|\,, \tag{5}$$

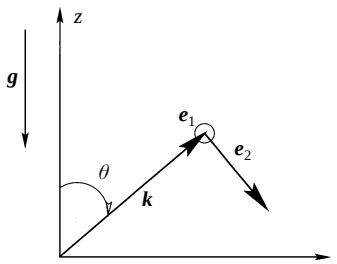

FIGURE 1. The Craya–Herring frame of reference ($\boldsymbol{e}^1$, $\boldsymbol{e}^2$, $\boldsymbol{k}$). The vector $\boldsymbol{e}^1$ is horizontal and perpendicular to the plane of figure.

and the last one, $\boldsymbol{e}^3(\boldsymbol{k}) = \boldsymbol{k}/k$, along $\boldsymbol{k}$, completes the frame. The vector $\boldsymbol{n}$ represents the vertical unit vector.

Note that the direction of $\boldsymbol{e}^2$ is the direction of steepest descent in the plane Π. This direction is exactly the one along which fluid particles oscillate in an internal wave (see figure 1). Thus, for a stably stratified flow, in the linear limit, the component of $\hat{\boldsymbol{u}}$ along $\boldsymbol{e}^2$, $\hat{\phi}^2$, coincides with the internal wave part. The component along $\boldsymbol{e}^1$ is the vortex part.

Regardless of physical considerations, decomposition (4) may simply be considered as a mathematical one and applied to a velocity field in any flow regime. This will be done here, for the whole duration of the simulated flows (from a turbulent regime to a weakly nonlinear one). However, whatever the flow stage, we shall improperly refer to $\hat{\phi}^1 e_i^1$ as the vortex part of the flow and to $\hat{\phi}^2 e_i^2$ as its internal wave part.

This decomposition can equivalently be formulated in physical space. Indeed, it amounts to splitting the velocity $\boldsymbol{u}$ into its horizontal and vertical components and to applying Helmholtz decomposition to the former component:

$$\boldsymbol{u} = \nabla_h \times \psi \boldsymbol{n} + \nabla_h \zeta + u_3 \boldsymbol{n} \tag{6}$$

where ∇_h represents the gradient operator in a horizontal plane. This decomposition is often used for compressible flows. As shown by Riley *et al.* (1981), for a stably stratified flow in the linear limit, the last two terms of (6) define the velocity field of the internal wave part while $\nabla_h \times \psi \boldsymbol{n}$ defines the non-propagating or vortex part of the flow. The latter part is thus characterized by its containing all of the vertical vorticity of the flow while the internal wave part contains all of the vertical velocity. The above decomposition can be extended to a weakly nonlinear regime by replacing the horizontal planes by (slightly tilted) isopycnals (Staquet & Riley 1989).

The scalar field ψ uniquely defines the vortex part of the flow. As well, the scalar field ζ uniquely defines the wave part of the flow when the velocity field is incompressible, since, in this case, u_3 and ζ are related by

$$\nabla_h^2 \zeta = -\frac{\partial u_3}{\partial x_3}, \tag{7}$$

where ∇_h^2 denotes the Laplacian operator in a horizontal plane. The latter result is consistent with a decomposition proposed by Hart (1981) in physical space, in terms of a single potential as well, for any velocity field satisfying the linearized incompressible Boussinesq equations.

Finally, it can be easily shown that decomposition (4) is equivalent to (6) for

an incompressible flow. Indeed, components $\hat{\phi}^1$ and $\hat{\phi}^2$ are related to the Fourier transforms of the scalar fields $\hat{\psi}$ and $\hat{\zeta}$ by

$$\hat{\phi}^1 = \mathrm{i}k_h\hat{\psi}, \quad \hat{\phi}^2 = \mathrm{i}\frac{k_h k}{k_z}\hat{\zeta} = -\frac{k}{k_h}\hat{u}_3. \tag{8}$$

3. The EDQNM$_2$ model for stratified turbulence

3.1. *Basics of the anisotropic EDQNM closure derivation*

In the EDQNM model, the hierarchy of equations for correlations of the velocity field at successive order is closed at third order, by assuming that the velocity distribution is not far from Gaussian. More precisely, the fourth-order correlations are expressed in terms of second-order ones, the fourth-order cumulant being modelled as a damping term of the third-order correlations. The reader is referred to classical works in the literature for details on the EDQNM model in the isotropic case (Orszag 1970; Herring & Kraichnan 1971; Lesieur 1990). We show hereafter the main lines of the derivation of an anisotropic version and adopt a formal presentation for clarity.

Cambon (1989) has proposed a general way of obtaining the statistical EDQNM closure for a velocity equation – or another vector variable such as the velocity–temperature one introduced in the following section – whereof the linear operator includes an additional term with respect to the dissipation term of the Navier–Stokes equations. Such a generic equation may be written as

$$\dot{\hat{\boldsymbol{v}}} + \boldsymbol{L}\hat{\boldsymbol{v}} = \underbrace{\int_{\boldsymbol{k}+\boldsymbol{p}+\boldsymbol{q}=0} \boldsymbol{M}(\boldsymbol{k},\boldsymbol{p},\boldsymbol{q})\hat{\boldsymbol{v}}(\boldsymbol{p})\hat{\boldsymbol{v}}(\boldsymbol{q})\,\mathrm{d}^3\boldsymbol{p}}_{\boldsymbol{b}(\boldsymbol{k})}\,, \tag{9}$$

where the time dependency has not been explicitly included in the right-hand side. The overdot indicates a time derivative. The tensor $\boldsymbol{M}$ contains the interaction coefficients between the Fourier modes $\hat{\boldsymbol{v}}(\boldsymbol{p})$ and $\hat{\boldsymbol{v}}(\boldsymbol{q})$, and represents the nonlinear terms. The solution of this equation can be written with the help of the Green's function of the linear operator $\boldsymbol{L}$, namely $\boldsymbol{G}$, that allows one to obtain the solution for the linear part of equation (9), given an initial condition $\hat{\boldsymbol{v}}(t_0)$. Namely, this yields

$$\hat{\boldsymbol{v}}(\boldsymbol{k},t) = \boldsymbol{G}(\boldsymbol{k},t-t_0)\hat{\boldsymbol{v}}(\boldsymbol{k},t_0) + \int \boldsymbol{G}(\boldsymbol{k},t-t')\boldsymbol{b}(\boldsymbol{k},t')\,\mathrm{d}t' \tag{10}$$

where $\mathbf{b}$ is the right-hand-side of equation (9). Given the formal solution (10) at any time, it is easy to obtain the solution of any particular nth-order moment $\boldsymbol{V}^{(n)}$ of variable $\boldsymbol{v}$ at any time t, owing to the fact that the Green's function for the linearized equation of this moment is but a product of n Green's functions $\boldsymbol{G}$. Each of these depends on a different wavevector, that lies among the n wavevectors on which the nth order moment depends. Thus, from the evolution equation of the triple correlations of $\hat{\boldsymbol{v}}$, which we write in a symbolic form:

$$\dot{\boldsymbol{V}}^{(3)} + \sum \boldsymbol{L}\boldsymbol{V}^{(3)} = \boldsymbol{V}^{(4)}\,, \tag{11}$$

one may obtain the formal solution for triple correlations in terms of the fourth-order ones. Here, the summation sign indicates sums over all possible permutations of indices of the second-order tensor $\boldsymbol{L}$ and the third-order one $\boldsymbol{V}^{(3)}$, i.e. representing different components of these tensors. This symbolic notation is used throughout this

section for denoting summations over the order of indices, such as the quasi-normal development of equation (12).

The modelling comes in at this step, where $\boldsymbol{V}^{(4)}$ is written in terms of the second-order moments, as in the isotropic EDQNM model, assuming that the distribution of the random variable $\boldsymbol{v}$ is close to a Gaussian one. Let us point out here that, as an extra assumption, we suppose that this property is also verified by the *temperature* variable, in addition to the velocity one. In so doing, we get the quasi-normal (QN) part of the closure model. As in the isotropic model, the eddy-damping (ED) part comes from a departure from the Gaussian development and takes into account the non-zero triple correlations, here again extending the argument to the temperature field. The quasi-Gaussian decomposition is

$$\boldsymbol{V}^{(4)} = \sum \boldsymbol{V}^{(2)}\boldsymbol{V}^{(2)} - \mu(\boldsymbol{k})\boldsymbol{V}^{(3)} \tag{12}$$

where μ is the eddy damping rate of the triple correlations by the fourth-order cumulant. One of the key issues of the EDQNM model is the choice of this damping rate. In our model, the classical damping rate is used for variable $\boldsymbol{v}$, $\mu(k) = A\ \int_0^k p^2 E(p)\,\mathrm{d}p$, that contains $A = 0.366$, the only adjusted – once and for all – constant of the model, to recover the Kolmogorov constant in the most simple test case (André & Lesieur 1977). The spectrum $E(k)$ is the spherically averaged kinetic energy spectrum. Putting (12) in (11) yields the equation for the third-order correlations:

$$\dot{\boldsymbol{V}}^{(3)} + \left(\sum \boldsymbol{L} + \mu\right) \boldsymbol{V}^{(3)} = \sum \boldsymbol{V}^{(2)}\boldsymbol{V}^{(2)}\,, \tag{13}$$

whereof the solution is

$$\boldsymbol{V}^{(3)}(\boldsymbol{k},\boldsymbol{p},\boldsymbol{q},t) = \boldsymbol{V}^{(3)}(\boldsymbol{k},\boldsymbol{p},\boldsymbol{q},t_0) + \int_{t_0}^{t} \mathrm{d}t' \int_{\boldsymbol{k}+\boldsymbol{p}+\boldsymbol{q}=0} \left[\boldsymbol{G}^{+}\boldsymbol{M}\right](\boldsymbol{k}) \left[\boldsymbol{G}^{+}\boldsymbol{V}^{(2)}\right](\boldsymbol{p}) \left[\boldsymbol{G}^{+}\boldsymbol{V}^{(2)}\right](\boldsymbol{q})\,\mathrm{d}^3\boldsymbol{p} \tag{14}$$

where the dependence of the right-hand-side terms on t and t' is skipped in our notation. The function $\boldsymbol{G}^{+}$ in the above equation is not exactly $\boldsymbol{G}$, since the *linear* eddy damping term in (12) introduces an extra part to the Green's function $\boldsymbol{G}$, such that

$$\boldsymbol{G}^{+}(\boldsymbol{k},t,t') = \boldsymbol{G}(\boldsymbol{k},t-t') \exp\left[-\int_{t}^{t'} \mu(\boldsymbol{k},t'')\,\mathrm{d}t''\right]\,. \tag{15}$$

The 'M' (for *Markovian*) of the EDQNM model refers to the way the time integration in equation (14) is performed, for dealing with the initial conditions. No difference with the original Markovian procedure has been introduced in our model. Finally, the solution (14) for $\boldsymbol{V}^{(3)}$ in the evolution equation for $\boldsymbol{V}^{(2)}$ putting

$$\dot{\boldsymbol{V}}^{(2)} + \sum \boldsymbol{L}\boldsymbol{V}^{(2)} = \boldsymbol{V}^{(3)}, \tag{16}$$

provides the closed equations for the double correlations. Obtaining the explicit model in terms of the wave part, vortex part, and temperature spectra is only a matter of switching to the local Craya–Herring reference frame.

The above constitutes a synoptic presentation of the way anisotropic EDQNM models can be constructed, not only considering the Boussinesq equations, but also including a Coriolis force (rotating turbulence) or an explicit Joule dissipation term (MHD turbulence) for instance, all of which appear as additional linear operators in the Navier–Stokes equations (Cambon & Godeferd 1993).

3.2. *Formulation of the EDQNM$_2$ model in the Craya–Herring frame*

For stably stratified flows within the Boussinesq equations, the variable $\hat{\boldsymbol{v}}(\boldsymbol{k},t)$ is a combination of the velocity and temperature fields:

$$\hat{v}_i(\boldsymbol{k},t) = \hat{u}_i(\boldsymbol{k},t) + \mathrm{i}\frac{k_i}{k}\frac{\hat{T}(\boldsymbol{k},t)}{N}. \tag{17}$$

Note that the scaled temperature $\hat{T}/N$ is considered to lie along the wavevector $\boldsymbol{k}$ so that $\hat{\boldsymbol{v}}$ is a three-component vector in Fourier space. The third component is denoted $\hat{\phi}^3$:

$$\hat{\phi}_i^3(\boldsymbol{k},t) = \frac{\hat{T}(\boldsymbol{k},t)}{N}. \tag{18}$$

Half the variance $\hat{\phi}_i^3\ \hat{\phi}_i^{3*}/2$ is simply the spectral density of the potential energy of the flow. The variable $\hat{\boldsymbol{v}}$ satisfies the property $\hat{v}_i^*\hat{v}_i/2 = \hat{u}_i^*\hat{u}_i/2 + \hat{T}^*\hat{T}/(2N^2)$, that is, half the variance of $\hat{\boldsymbol{v}}$ is the spectral density of the total energy (kinetic+potential).

As just seen, the EDQNM$_2$ model is expressed in terms of the double correlations $\boldsymbol{V}^{(2)}$ of $\hat{\boldsymbol{v}}$. The projection of $\boldsymbol{V}^{(2)}$ onto the different axes of the Craya–Herring frame provides the different correlation spectra for the components of $\hat{\boldsymbol{v}}$ in the local frame:

$$\tfrac{1}{2}e_i^u V_{ij}^{(2)} e_j^v = \begin{pmatrix} \Phi_1 & 0 & 0 \\ 0 & \Phi_2 & \Psi^* \\ 0 & \Psi & \Phi_3 \end{pmatrix}; \tag{19}$$

$\Phi_i(\boldsymbol{k},t) = \left\langle \hat{\phi}^{i*}\hat{\phi}^i \right\rangle /2$ is the energy spectrum of the vortex part ($i=1$), of the wave part ($i=2$) and of the potential energy ($i=3$). $\Psi = \left\langle \hat{\phi}^{2*}\hat{\phi}^3 \right\rangle /2$ is the correlation spectrum. $\langle\ \rangle$ denotes an ensemble average. The integration along the vertical direction of the real part of Ψ, denoted Ψ_R, leads to the vertical heat flux

$$\tfrac{1}{2}\langle wT\rangle = -N\int \Psi_R(\boldsymbol{k})\sin\theta_k \mathrm{d}^3\boldsymbol{k}. \tag{20}$$

Using equations (14), (15) and (16), we obtain the EDQNM$_2$ model within the Craya–Herring frame:

$$[\partial/\partial t + 2\nu k^2]\Phi_1(\boldsymbol{k},t) = \mathscr{T}^1(\boldsymbol{k},t), \tag{21}$$

$$[\partial/\partial t + 2\nu k^2]\Phi_2(\boldsymbol{k},t) + N\sin\theta_k\Psi_R(\boldsymbol{k},t) = \mathscr{T}^2(\boldsymbol{k},t), \tag{22}$$

$$[\partial/\partial t + 2\nu k^2]\Phi_3(\boldsymbol{k},t) - N\sin\theta_k\Psi_R(\boldsymbol{k},t) = \mathscr{T}^3(\boldsymbol{k},t), \tag{23}$$

$$[\partial/\partial t + 2\nu k^2]\Psi_R(\boldsymbol{k},t) - 2N\sin\theta_k[\Phi_2(\boldsymbol{k},t) - \Phi_3(\boldsymbol{k},t)] = \mathscr{T}^{\Psi_R}(\boldsymbol{k},t), \tag{24}$$

$$[\partial/\partial t + 2\nu k^2]\Psi_I(\boldsymbol{k},t) = \mathscr{T}^{\Psi_I}(\boldsymbol{k},t)\ . \tag{25}$$

The equation for the imaginary part of the velocity–temperature correlation Ψ_I is totally decoupled from the others, and leads to a constant zero spectrum $\Psi_I(\boldsymbol{k})$, if it is initially zero. We shall make this assumption in the following and thus ignore equation (25). Equations (21)–(24) are our EDQNM$_2$ model.

The modelled transfer terms in the right-hand sides of equations (21)–(24) are denoted with script letter $\mathscr{T}$. Their full expression in provided in the Appendix. Note that the left-hand sides of equations (21)–(24) are the same as those appearing in the corresponding exact equations, using the wave and vortex spectra formulation. The

only difference lies in the nonlinear transfer terms that would contain the unmodelled third-order correlations.

The modelled transfer terms are of the form

$$\mathscr{T}_{ij}(\boldsymbol{k},t) = \sum_{(\varepsilon\varepsilon'\varepsilon'')\in\{0,\pm1\}^3} \mathscr{T}_{ij}^{\varepsilon\varepsilon'\varepsilon''}(\boldsymbol{k},t) \tag{26}$$

with

$$\mathscr{T}_{ij}^{\varepsilon\varepsilon'\varepsilon''}(\boldsymbol{k},t) = \int_{\boldsymbol{k}+\boldsymbol{p}+\boldsymbol{q}=0} \frac{S_{ij}^{\varepsilon\varepsilon'\varepsilon''}(\boldsymbol{k},\boldsymbol{p},\boldsymbol{q})}{\tau_{kpq}^{-1} - \mathrm{i}N(\varepsilon\sin\theta_k + \varepsilon'\sin\theta_p + \varepsilon''\sin\theta_q)}\,\mathrm{d}^3\boldsymbol{p}\ . \tag{27}$$

The tensor $\boldsymbol{S}^{\varepsilon\varepsilon'\varepsilon''}$ contains many terms, with geometrical coefficients and the energy spectra. The transfer terms $\mathscr{T}_{ij}^{\varepsilon\varepsilon'\varepsilon''}$ are obtained by simple projection operations on the Craya–Herring frame.

The decomposition of the nonlinear transfer terms in (26) and (27) allows one to identify the various contributions, coming from different types of interactions in the flow, among vortex parts, wave parts, or between wave and vortex parts. Indeed, when the indices ε, ε' or ε'' are equal to $+1$ or -1, the part of the motion that is involved in the triadic interaction is internal waves with wavevectors $\boldsymbol{k}$, $\boldsymbol{p}$ and $\boldsymbol{q}$, propagating either in the one direction or its opposite, depending on the sign of the index. For the zero-valued indices, the vortex part is considered in the triadic interaction, with the corresponding wavevector.

Definition (27) shows that the effective damping rate of the triple correlations is

$$\tau_{kpq}^{-1} - \mathrm{i}N(\varepsilon\sin\theta_k + \varepsilon'\sin\theta_p + \varepsilon''\sin\theta_q). \tag{28}$$

Its real part τ_{kpq}^{-1} is the damping rate of the triple correlations that comes from the application of the isotropic closure assumption to $\boldsymbol{v}$ (see previous section): $\tau_{kpq}^{-1} = \nu(p^2+q^2+k^2)+\mu(k)+\mu(p)+\mu(q)$. The imaginary part results from the presence of an additional term – due to the stable stratification – in the linear operator acting upon $\boldsymbol{v}$. It is important to underline that this imaginary part appears naturally from our way of deriving the model, and not from any extra assumption. The triple product of Green's functions in equation (14) leads to the appearance of the resonance condition for wave interactions, exactly as it appears in a weakly nonlinear analysis dealing with a unique triad of vectors $\boldsymbol{k}$, $\boldsymbol{p}$, $\boldsymbol{q}$ (Lelong & Riley 1991). The only difference in the two approaches, at this level, comes from our dealing with full turbulence, so that we have to integrate the triadic interactions over the complete spectrum of the flow velocity field.

Thus, the level of the energy transfer relative to the isotropic situation depends on the value of $N(\varepsilon\sin\theta_k + \varepsilon'\sin\theta_p + \varepsilon''\sin\theta_q)$. If the resonance condition is met, i.e. if the previous sum of frequencies is zero, the triple correlations are damped with the same rate as in isotropic turbulence. The triads then involve either vortex motions only, resonant internal waves only, or internal waves resonantly interacting with one vortex (Lelong & Riley 1991). On the other hand, when the resonance condition is not fulfilled, the stratification acts as a scrambling effect proportional to N, since the corresponding term is purely imaginary. It follows that energy transfers are (mainly) ensured by resonant interactions. Note also that, since we deal with continuous spectra of statistical turbulence, the integral of all contributing interactions from different scales and modes of motion in the flow is computed to get the evolution of the spectra.

3.3. *Notation*

To avoid confusion, we shall denote by $(\phi^1(\boldsymbol{k},t),\phi^2(\boldsymbol{k},t))$ the components of $\boldsymbol{u}(\boldsymbol{k},t)$ in Fourier space; by $(\Phi_1(\boldsymbol{k},t),\Phi_2(\boldsymbol{k},t))$ the variance – or kinetic energy spectrum – of each component; by $(\Phi_1(k,t),\Phi_2(k,t))$ the spherically averaged variance – or energy density spectrum – of each component; and by $(\Phi_V(t),\Phi_W(t))$ the volume-averaged kinetic energy in the vortex and wave parts. As well, $\phi^3(\boldsymbol{k},t)$, $\Phi_3(\boldsymbol{k},t)$, $\Phi_3(k,t)$ and E_p will denote respectively the third component of $\mathbf{v}(\boldsymbol{k},t)$, its variance (or potential energy spectrum), the potential energy density spectrum and the volume averaged potential energy.

4. Numerical method, initial condition and physical parameters

4.1. *Numerical method*

4.1.1. *Direct numerical simulations*

The system of equations (1) has been solved with periodic boundary conditions in all three directions, using a pseudo-spectral method. In order to ensure numerical stability, the nonlinear terms are rewritten in rotation form prior to solving, using the identity $(\boldsymbol{u}\cdot\nabla)\boldsymbol{u} = \omega\times\boldsymbol{u} + \frac{1}{2}\nabla|\boldsymbol{u}^2|$ (e.g. Canuto *et al.* 1988, pp. 116 and 208); $\boldsymbol{\omega} = \nabla\times\boldsymbol{u}$ is the vorticity. In a pseudo-spectral method, the spatial derivatives are computed in Fourier space while the nonlinear terms are computed in physical space. A standard truncation procedure is applied to the fields before computing the nonlinear product so as to avoid aliasing effects. Time marching is done using a third-order Adams–Bashforth scheme, and the viscous term is integrated exactly using the new variable $\boldsymbol{u}(\boldsymbol{k})\exp(\nu k^2 t)$. The computational domain is a cubic box of side 2π, 4π or 8π (see table 1). The resolution is 256^3 and comparison with simulations of lower resolution, 128^3, will be made.

4.1.2. *Numerical resolution of the* EDQNM_2 *model*

To solve numerically the system of equations (21) – (24), we first reduce the last three equations into two equations, for an oscillating (complex) quantity $Z = \Phi_2-\Phi_3+\mathrm{i}\Psi_R$ and for a non-oscillating (real) quantity $\Phi_2+\Phi_3$. The explicit stratification term becomes thus isolated into one equation, for Z. The linear terms in all equations are solved exactly by using integrating factors that include either both the viscous decay and the stratification term, as in the Z equation, or only the viscous dissipation term, as in the equations for the non-oscillating quantities Φ_1 and $\Phi_2+\Phi_3$. The $\partial/\partial t$ remaining time-dependent terms are then integrated by an explicit Euler time scheme. In the isotropic case, we have checked that no significant improvement in accuracy can be obtained over the time intervals of interest, by increasing the order of the time-advancement scheme (we used a third-order Adams–Bashforth scheme).

The numerical calculation of the triadic integrals in equation (27) is performed as a discretized integral in terms of spherical coordinates, i.e. a summation over all wavenumbers and angles, with a linear interpolation to compute the spectra at wavevector $\boldsymbol{q}$ ($\boldsymbol{q} = -\boldsymbol{k}-\boldsymbol{p}$ with given discretized $\boldsymbol{k}$ and $\boldsymbol{p}$). The minimum and maximum wavenumbers are the same as in the DNS: for instance, for a 256^3 simulation of domain side $n2\pi$, $k_{min} = 1/n$ and $0 \leqslant k/k_{min} \leqslant 128$. The angle of $\boldsymbol{k}$ with vertical is discretized into 19 angles from 0 to $\pi/2$.

The EDQNM_2 calculations are easily parallelized. The time advancement scheme being explicit, the discretized equations (21)–(24) amount to expressing the spectra at iteration $(n+1)$ as a function of the known spectra at iteration n, through linear

and nonlinear terms. The parallelization process uses the fact that these terms depend upon the wavevector $\boldsymbol{k}$ so that their computation can be dispatched over different computational nodes. Theoretically, one could use as many computational nodes as discretized wavenumbers, with a speedup almost as high as the number of nodes. Most of the EDQNM$_2$ results presented in the following have been obtained on a cluster of eight workstations.

4.2. *Initial condition*

The procedure we use to initialize the velocity and density fields of the stably stratified flow in the DNS has now become classical (Orszag & Patterson 1972). In a preliminary stage, a homogeneous turbulent non-stratified flow is created via a so-called 'isotropic pre-simulation'. This DNS is initialized with a narrowband spectrum of kinetic energy density

$$E(k) = 16\left(\frac{2}{\pi}\right)^{1/2} u_0^2 k^4 \exp\left[-2\left(\frac{k}{k_0}\right)^2\right]. \tag{29}$$

One realization of the velocity field is obtained by defining this field in Fourier space: for each wavevector $\boldsymbol{k}$, the amplitude is deduced from $E(k)$ and the phase is initialized by a random generator with uniform distribution. In the DNS presented in this paper, the peak of the spectrum is located at wavenumber $k_0 = 4.76$ (the side of the computational box being 2π, 4π or 8π) and its magnitude is such that $u_0^2 \equiv \overline{u_1^2} = \overline{u_2^2} = \overline{u_3^2} \simeq 1$, where the overbar denotes a volume average. The initial triple correlations for the velocity field are therefore zero. This DNS is carried out up to the time, denoted t_0, at which three conditions are satisfied: energy has been transferred to the smallest scales; the skewness factor is about 0.4; and $\Phi_V = \Phi_W$ (the spherically averaged energy density spectra $\Phi_1(k, t_0)$ and $\Phi_2(k, t_0)$ are thus very close, for any k). Therefore, the flow is close to a homogeneous isotropic turbulent flow. In practice, t_0 varies between 0.75 and 0.94 for the different calculations.

A stably stratified flow is created at $t = t_0$ by setting N to a non-zero value. The potential energy at that time is chosen so that, for any k, $\Phi_3(k, t_0) = \Phi_2(k, t_0)$. As said in Introduction, this choice is motivated by the validation of the closure assumption of the EDQNM$_2$ model. Indeed, equation (24) shows that, in this case, the spectrum $\psi_R(\boldsymbol{k}, t)$ becomes driven by the nonlinear transfer term $\mathscr{T}^{\Psi_R}$, at least in the early stage of the flow. Therefore, if $\Psi_R(\boldsymbol{k}, t)$ is zero at $t = t_0$, the temporal evolution of Φ_2 and Φ_3 will be mainly controlled by the nonlinear transfer terms $\mathscr{T}^2$ and $\mathscr{T}^3$ respectively. We therefore expect that $\psi_R(\boldsymbol{k}, t)$, if zero at $t = t_0$, will remain weaker during this early stage than for the usual initial conditions made a reservoir of either kinetic energy or potential energy. The flow dynamics in our calculations should therefore be most sensitive to the modelling of the nonlinear transfer terms, which involves the closure assumption.

The comparison between the EDQNM$_2$ model and the DNS is initiated as follows. The DNS spectra $\Phi_1(k)$, $\Phi_2(k)$ and $\Phi_3(k) = \Phi_2(k)$ at $t = t_0$ are used to initialize the EDQNM$_2$ model (Ψ_R is set to zero at that time in the model). In the numerical simulations, a deterministic temperature field is defined in Fourier space from $\Phi_3(k)$, with the addition of random phases. The physical parameters (the viscosity ν and the Brunt–Väisälä frequency N) are the same in the EDQNM$_2$ model and in the simulations. We recall that $Pr = 1$ for all calculations.

A DNS corresponds to a given realization of the flow while the predictions of the statistical EDQNM$_2$ model are those for an ensemble average. Before proceeding

Run	Resolution	Duration of run (from t_0)	ν	N	Side of the computational domain	Fr_t at $t = t_0$	Re_λ at $t = t_0$
A	256^3	$3T_{BV}$	1/400	π	2π	0.38	58
B	256^3	$3T_{BV}$	1/400	π	2π	0.38	58
C	256^3	$3T_{BV}$	1/400	π	2π	0.38	58
D	256^3	$3T_{BV}$	1/400	π	2π	0.38	58
R0	256^3	$6T_{BV}$	1/300	0	4π	NA	45
R1	256^3	$6T_{BV}$	1/300	$\pi/2$	4π	0.88	45
R2	256^3	$6T_{BV}$	1/300	π	4π	0.44	45
R3	256^3	$6T_{BV}$	1/500	π	4π	0.45	57
R4	256^3	$6T_{BV}$	1/150	π	8π	0.45	32
r0	128^3	$6T_{BV}$	1/150	0	4π	NA	32
r1	128^3	$6T_{BV}$	1/150	$\pi/2$	4π	0.91	32
r2	128^3	$6T_{BV}$	1/150	π	4π	0.45	32
c2	128^3	$3T_{BV}$	1/300	π	2π	0.33	56

TABLE 1. Sets of parameters for the different runs of DNS and of EDQNM$_2$ calculations. ν is the kinematic viscosity and N the Brunt–Väisälä frequency. t_0 is the time at which N is set to a non-zero value in the pre-simulation of isotropic homogeneous turbulence. Fr_t, defined by (33) is a turbulent Froude number, while Re_λ, defined by (34), is a Reynolds number based upon the Taylor microscale.

to the comparison between DNS and EDQNM$_2$, it is necessary to examine the variability of the DNS results as a function of the random phase realizations (used to initialize the velocity field at $t = 0$ and the temperature field at $t = t_0$). For this purpose, four 256^3 DNS have been run over three Brunt–Väisälä periods. These DNS are denoted A, B, C, and D in table 1 and their features are described there. We solely focus upon the fact that simulations A, B and C stem from the same isotropic pre-simulation and differ in the realization of the temperature field at $t = t_0$, while the velocity field in simulation D is initiated by a different isotropic pre-simulation. In figure 2(*a*), the total energy (kinetic+potential) is plotted as a function of time. The four curves remain very close as time elapses, the maximum relative difference reaching 3 % only after $3T_{BV}$. The origin of this relative difference is clarified when the kinetic energy of the vortex part Φ_V and of the wave part Φ_W are examined (figures 2(*b*) and 2(*c*)). For the former quantity, the four curves almost superpose, the relative difference being at most 1%. Figure 2(*c*) shows that the differences in the total energy should be attributed to the latter quantity, namely the wave part, simply because the oscillations of the internal waves are not in phase, due to the different random realizations of either the velocity field initiating the isotropic pre-simulation, or the temperature field at $t = t_0$. However, these minor differences are not dynamically significant. Thus, a single DNS realization can be compared to an EDQNM$_2$ calculation when volume-averaged energies are to be studied.

In figure 2(*d*), the normalized heat flux (correlation coefficient between the vertical velocity and the temperature fluctuation) is plotted for the four DNS. The four curves display about the same amplitude but their phases progressively shift from about one Brunt–Väisälä period (as was already visible in figure 2*c*) because of the different random realizations. The signals lose their relative coherence after $\simeq 1.5T_{BV}$. Hence, no attention should be paid to the phase of the wave oscillations when comparison

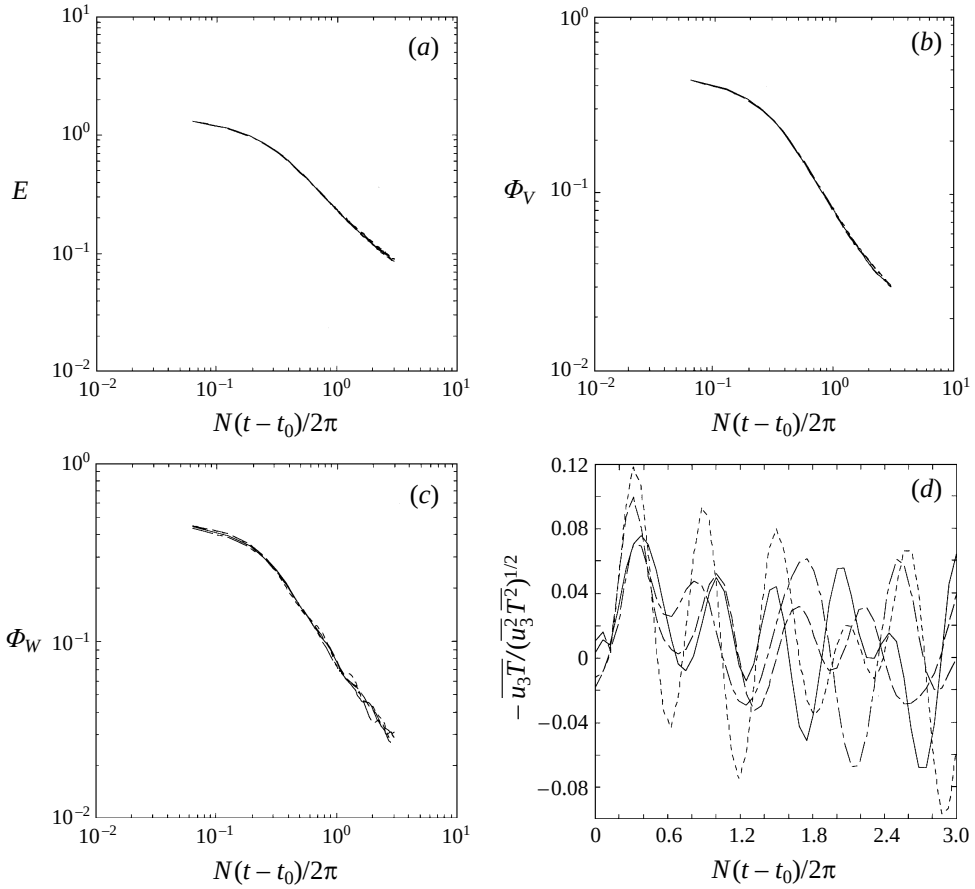

FIGURE 2. DNS results. Time evolution for runs A, B, C and D of (*a*) the total energy (kinetic+potential); (*b*) the vortex kinetic energy; (*c*) the wave kinetic energy; (*d*) the normalized vertical heat flux. t_0 is the initial time of the calculations with stable stratification. Time is non-dimensionalized by the Brunt–Väisälä period $T_{BV} = 2\pi/N$. —— run A; ---- run B; – – – run C; – – – – run D.

with the EDQNM$_2$ model will be made. Only the amplitude of the oscillations should be considered.

4.3. *Physical parameters*

The calculations discussed in the present paper are listed in table 1. As already noted, all stratified DNS are initialized by an isotropic pre-simulation. The viscosity is kept constant and has the same value in the pre-simulation and subsequent stratified DNS. This value is chosen so that the Kolmogorov scale

$$\eta = (\nu^3/\epsilon)^{1/4}, \tag{30}$$

is a few times less than the grid size ds at $t = t_0$: $\eta = \alpha\,\mathrm{d}s$, with $\alpha < 1$; ϵ is the volume-averaged dissipation rate of kinetic energy. The Kolmogoroff scale characterizes the scale at which energy is dissipated and, in practice, $\alpha = 1/3$ ensures that the smallest scales of the flow are properly resolved at $t = t_0$. The latter criterion will also be true at any subsequent time since η increases as time elapses (see figure 4*b*). Indeed, in a stably stratified flow, the transfer rates of (kinetic and potential) energy toward small

scales decrease as time elapses (e.g. Riley *et al.* 1981; Kimura & Herring 1996) and so does also ϵ, consequently. Note that the equation for the total energy is always satisfied to better than 1% from $t = t_0$ with the value of the viscosity obtained with this criterion.

Two stably stratified DNS will be extensively discussed in this paper, referred to as R1 and R2 in table 1. These DNS solely differ by the value of the Brunt–Väisälä frequency, either equal to $\pi/2$ or π. From a dynamical point of view, the Froude number $Fr = U/NL$ accounts for the importance of nonlinear effects, estimated by U/L, relative to stratification effects, estimated by N. U and L are characteristic velocity and length scales, which are specified below. Whatever the initial value of the Froude number in a stably stratified decaying turbulent flow, it always decreases below 1 as time elapses indicating that the flow supports successively all regimes, from a strongly nonlinear regime ($Fr > 1$) to a weakly nonlinear one ($Fr \ll 1$). The reason is that the characteristic time scale of nonlinear effects L/U increases with time, because the kinetic energy decreases, so that L/U becomes much larger than N^{-1} as time elapses. In runs R1 and R2, the values chosen for N yield a value of the Froude number of order 1 at $t = t_0$, as we show now, so that stratification effects are already strong at that time.

There are different ways to define the Froude number but it is generally expressed as the ratio of two length scales (e.g. Hopfinger 1987; LVA; YW). One of them is the buoyancy length scale

$$L_b = (\overline{u_3^2})^{1/2}/N \tag{31}$$

which is the greatest distance a fluid particle can move vertically against the temperature gradient. In the present case, L_b will be compared to an integral length scale L

$$L = (\overline{u_1^2})^{3/2}/\epsilon, \tag{32}$$

so that

$$Fr_t = L_b/L \tag{33}$$

is usually referred to as a turbulent – or overturning – Froude number. In equation (32), L represents the size of the most energetic eddies (this definition stems from the equation for the kinetic energy in an isotropic flow).

Fr_t computed by DNS for runs R1 and R2 is plotted in figure 3(*a*). The Froude number decays from about 1 down to 0.025, indicating that a quasi-linear regime is reached at $6T_{BV}$. The integral length scale L increases by a factor 3 during the simulations (not shown) so that the decay of Fr_t reflects a strong decrease of the vertical kinetic energy. Both curves in figure 3(*a*) start to match from about $0.5T_{BV}$, indicating that the Froude number behaviour becomes driven by buoyancy effects from this time on. This result is in agreement with experimental results of YW and LVA: the turbulent Froude number is compared for both sets of experiments in YW's article (their figure 18) and all data collapse on the same curve from $\simeq 0.5T_{BV}$. The value found by these authors at $0.5T_{BV}$ is reproduced for comparison in our figure 3(*a*). This value lies close to our curves, which suggests that the Froude number evolution also quickly becomes independent of the initial condition.

Fr_t predicted by the EDQNM$_2$ model and computed from the DNS is plotted in figure 3(*b*), for run R2. A very good agreement is found between both evolutions, apart from a slight underestimation by the EDQNM$_2$ model (by 20% at most). As shown below, this discrepancy stems from the energy in the u_1 component, which is overestimated by the EDQNM$_2$ model.

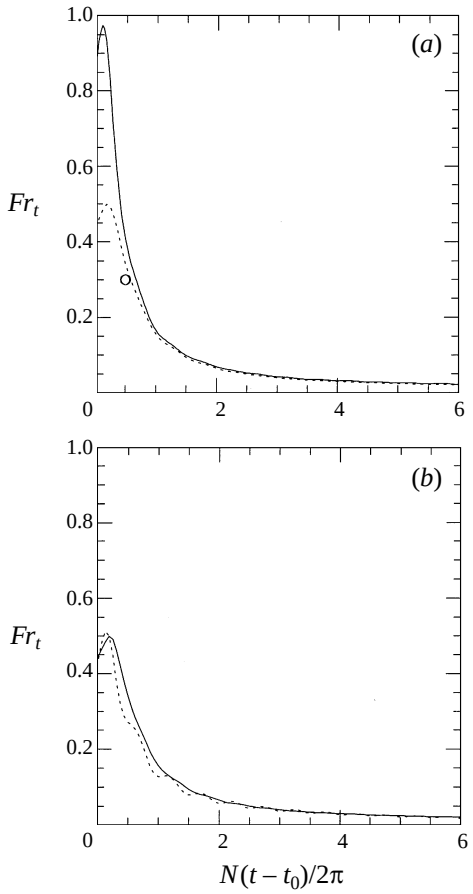

FIGURE 3. Time evolution of the Froude number Fr_t (defined by (33)). (*a*) DNS results. ——, run R1; - - - -, run R2; ○ indicates one value extracted from the experiments of Yoon & Warhaft (1990) and Lienhardt & Van Atta (1990). (*b*) Run R2 only. ——, DNS; - - - -, EDQNM$_2$ model.

The second dynamical parameter of the flow is a Reynolds number. Its definition is most often based upon the Taylor microscale λ

$$Re_\lambda = (\overline{u_1^2})^{1/2}\lambda/\nu, \tag{34}$$

with

$$\lambda = (10\nu E_k/\epsilon)^{1/2}. \tag{35}$$

E_k is the volume-averaged kinetic energy $\frac{1}{2}\sum_i \overline{u_i^2}$. Our high-resolution numerical simulations permit the attainment of the same initial value of Re_λ as in the wind tunnel experiments of YW and LVA, which is about 40. λ is about constant during the first half-Brunt–Väisälä period (see figure 4*b*) so that the strong decay of Re_λ reflects that of $\overline{u_1^2}$ (due to nonlinear transfers toward small scales). Re_λ seems to eventually reach an asymptotic constant value from $3T_{BV}$, close to 30 for run R2.

Figure 4(*a*) shows that the EDQNM$_2$ model overestimates Re_λ by about 6%. However, λ is remarkably well predicted by the EDQNM$_2$ model (see figure 4*b*). The discrepancy in Re_λ thus stems again from the energy in the u_1 component, as for the turbulent Froude number discussed above.

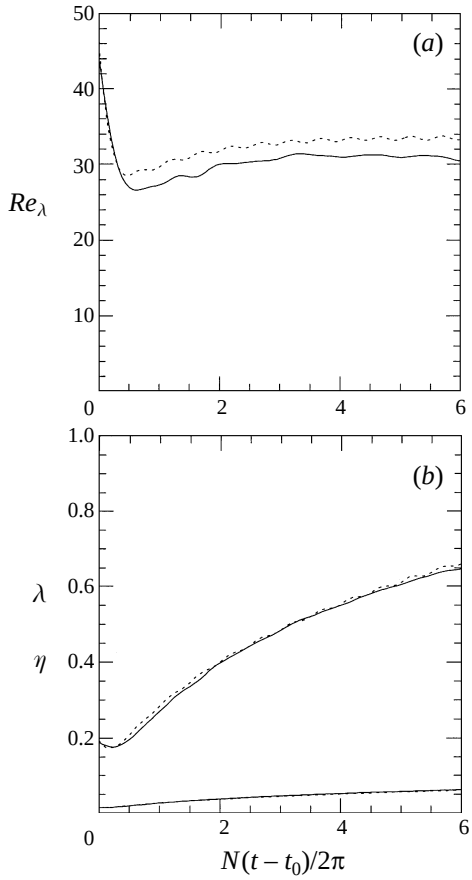

FIGURE 4. Run R2. (*a*) Reynolds number Re_λ based on the Taylor microscale λ: ——, DNS; - - - -, EDQNM$_2$ model. (*b*) Taylor microscale λ (top curves) and Kolmogorov microscale η (bottom curves): ——, DNS; - - - -, EDQNM$_2$ model.

The Kolmogorov scale defined by (30) is also displayed for the EDQNM$_2$ model and the DNS, in figure 4(*b*). A very good agreement is found up to $6T_{BV}$, implying that both approaches predict the same dissipation rate of kinetic energy. A detailed study of ϵ is presented in § 5.5.

5. Energetics of the flow: EDQNM$_2$ model versus DNS

5.1. *Total energy*

5.1.1. *DNS results*

The decay of the total energy (kinetic+potential) averaged over the computational domain $E(t)$ is examined in figure 5(*a*), for $N = \pi$. The isotropic pre-simulation has been continued beyond the time t_0 and its volume-averaged kinetic energy is plotted for comparison. The total energy is also plotted for stratified DNS having different values of the viscosity, so that the influence of this parameter can be estimated. All energies are normalized by their respective value at $t = t_0$.

Figure 5(*a*) shows that the overall decay of the total energy displays two stages. During the first Brunt–Väisälä period, the decay rate of the total energy is greater

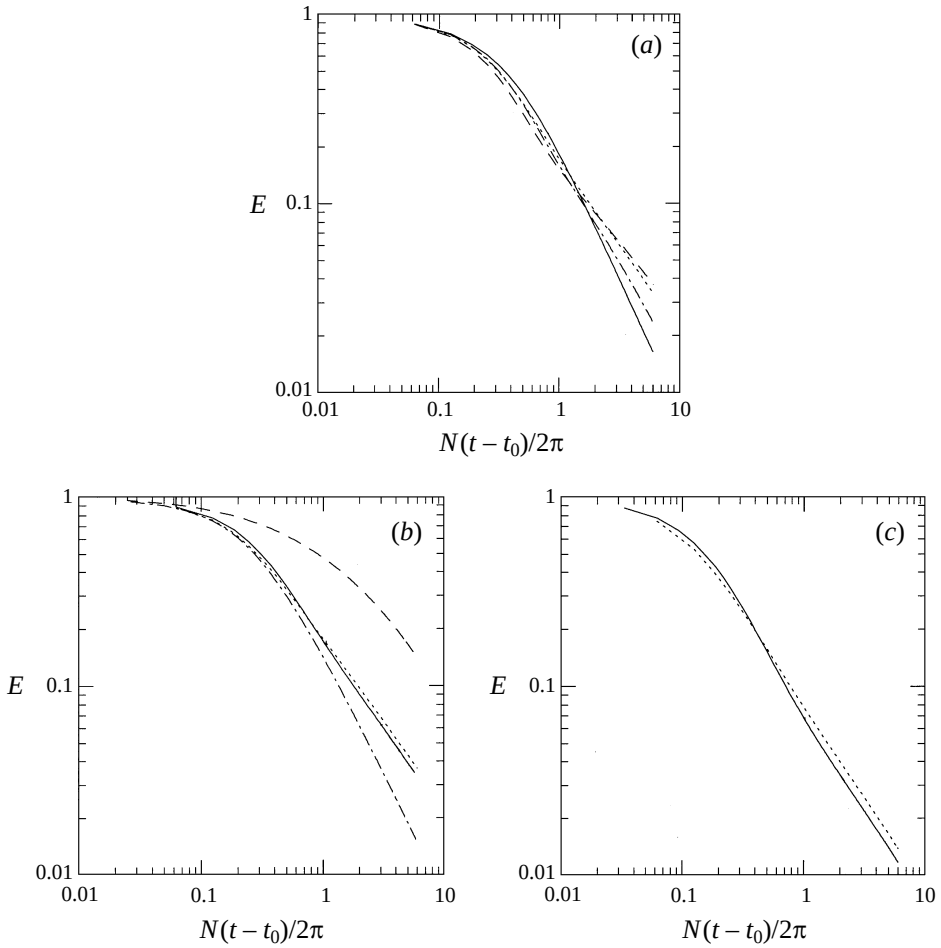

FIGURE 5. Total energy E (kinetic + potential). (*a*) DNS results: ——, run R0; – – –, run r2; - - -, run R2; – – – –, run R3. (*b*) Parameters of run R2, for: ——, DNS; - - - -, $EDQNM_2$ model; – – –, simplified $EDQNM_1$ model; – – – –, linear approximation (rapid distorsion theory). (*c*) Parameters of run R1 for: ——, DNS; - - - -, $EDQNM_2$ model.

than its isotropic counterpart. This surprising result is accounted for by the potential energy behaviour: a higher transfer of potential energy than of kinetic energy toward small scales occurs during this first period, as shown in the next subsections. The same behaviour is well-known to hold for a passive scalar. One argument proposed by Holloway (1988) is that the nonlinear interactions among the velocity field contain the subset of two-dimensional interactions, for which transfers toward small scales are forbidden by the nonlinear conservation of the vorticity (in two dimensions). By contrast, no such subset exists among the nonlinear interactions of the temperature field.

The total and isotropic energy levels reverse between one and two Brunt–Väisälä periods. This is a clear manifestation of the inhibition of nonlinear transfers of energy by the stable stratification. One way to account for this effect is to notice that, when $N = 0$, all triads can be designated as resonant since the frequency of any wavevector is zero. Hence, any wavevector can exchange its energy within a triad. When N is non-zero by contrast, the Froude number Fr_t reaches a value much smaller than 1 ($\simeq 0.15$) in about one Brunt–Väisälä period (see figure 3). Fr_t is associated with the

large scales of the flow, so that the energy at these scales can be considered as being distributed among weakly interacting gravity waves (coexisting with large-scale vortex motions, whereof the dynamics are quasi-two-dimensional). This energy should thus be transferred from large to small scales through mostly resonant, and thus selective, interactions (Phillips 1977). Another way to account for the inhibition of nonlinear transfers is to notice that these transfers depend upon the vertical velocity; but the vertical kinetic energy is converted into potential energy, which is partly involved in the irreversible process of fluid mixing.

Figure 5 (*a*) shows that the effects just described are more pronounced when the viscosity is smaller: the total energy for $\nu = 1/500$ has the lowest level for times smaller than T_{BV} but the highest level after one Brunt–Väisälä period. This suggests that some limit behaviour may be reached at infinitely small viscosity. Figure 4 also shows that viscous effects, if too strong, hide this behaviour, though their general influence on the flow is to stabilize it, as stratification does.

5.1.2. *Comparisons with the* EDQNM$_2$ *model*

The total energy for $N = \pi$ computed by the DNS and by the EDQNM$_2$ model is plotted in figure 5 (*b*). Apart from a 5% maximal overestimation, the prediction of the EDQNM$_2$ model matches the DNS result very well. These curves lie in between two other theoretical predictions, by the rapid distortion theory (RDT) and by the simplified EDQNM$_1$ model discussed in the Introduction. The RDT can be seen as the linear approximation of the EDQNM$_2$ and EDQNM$_1$ models. The RDT energy level is well above the DNS level: this demonstrates that the total energy for run R2 is controlled by nonlinear transfers, despite their weakening by the stable stratification. By contrast, the level of the total energy predicted by the simplified EDQNM$_1$ model is below the DNS and EDQNM$_2$ levels; the EDQNM$_1$ energy level actually follows quite closely that of the non-stratified counterpart flow. This shows that an isotropic closure assumption is not suitable to model the large-scale behaviour of the flow.

5.2. *Kinetic and potential energy*

The horizontal and vertical kinetic energies, E_h and E_v, and the potential energy E_p are plotted versus time in figure 6. The DNS results and the EDQNM$_2$ model predictions are compared for runs R1 and R2. E_h and E_v are respectively defined by $E_h = \frac{1}{2}(\overline{u_1^2} + \overline{u_2^2})$ and $E_v = \frac{1}{2}\overline{u_3^2}$. For a uniform stratification, a good approximation of the potential energy of the temperature fluctuations (or 'available potential energy') is

$$E_p = \tfrac{1}{2}\overline{T^2}/N^2 \tag{36}$$

(e.g. Holliday & McIntyre 1981). The initial levels of E_h, E_v and E_p are dictated by the initial condition we have chosen:

$$E_p(t_0) = \tfrac{3}{2}E_v(t_0) = \tfrac{3}{4}E_h(t_0). \tag{37}$$

This situation contrasts with laboratory experiments by YW and LVA, where E_p is at most 1% of E_v at the first measuring station (corresponding to $\simeq 0.05T_{BV}$).

A first inspection of the curves in figure 6 reveals a very good agreement between the EDQNM$_2$ predictions and DNS results. In particular, the decay rate of all three curves is correctly predicted by the model. A more detailed examination reveals some discrepancy however. The amplitude of the oscillations for the potential energy and vertical kinetic energy, which are contributed solely by the wave part of the flow, is overestimated by the EDQNM$_2$ model. This trend is shared by both flows but is

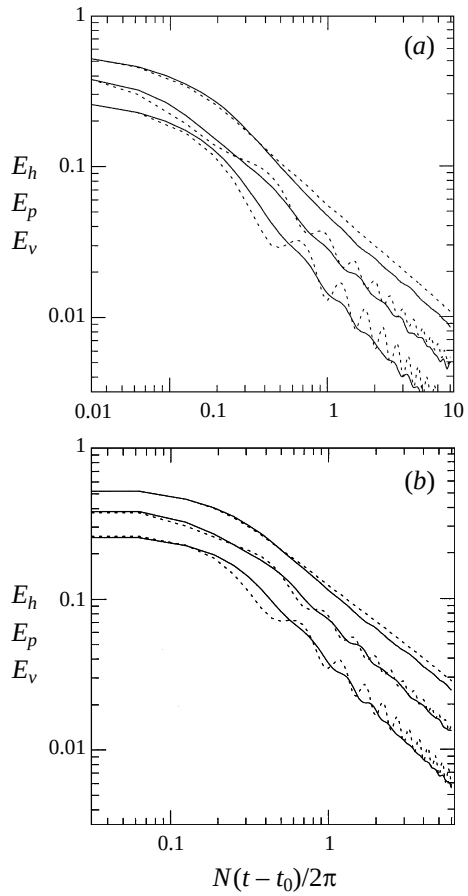

FIGURE 6. Time evolution of the horizontal kinetic energy (top curves), the potential energy (middle curves), and the vertical kinetic energy (bottom curves); —— DNS; - - - - EDQNM$_2$ model. (*a*) run R1; (*b*) run R2.

more pronounced for run R1. Though hardly visible on the curves presented in figure 6, the amplitude of the oscillations computed by the DNS is also larger for run R1. One argument is provided below to account for this effect. Figure 6 also shows that the level of the potential energy is well predicted by the EDQNM$_2$ model while that of E_v is slightly overpredicted.

The horizontal kinetic energy decays at a lower rate than the two other energies suggesting that it is associated with larger-scale motions. Also, E_h displays oscillations of very weak amplitude. Since the vortex part of the flow is solely horizontal, by definition, this implies that the wave contribution to E_h should remain weak at all times. We have found that 70 % of E_h is indeed contributed by Φ_V, the vortex kinetic energy. The level of the horizontal kinetic energy is overestimated by the EDQNM$_2$ model, the relative difference reaching 15% after $6T_{BV}$ for run R1. Note however that, for a given number of Brunt–Väisälä periods, this run has been carried out over twice the duration of run R2. Hence, some confinement effect may have arisen in the DNS for run R1 (that is, the largest scales of the flow, which grow as time elapses, may become influenced by the domain boundaries). The influence of a confinement effect is discussed in § 6.

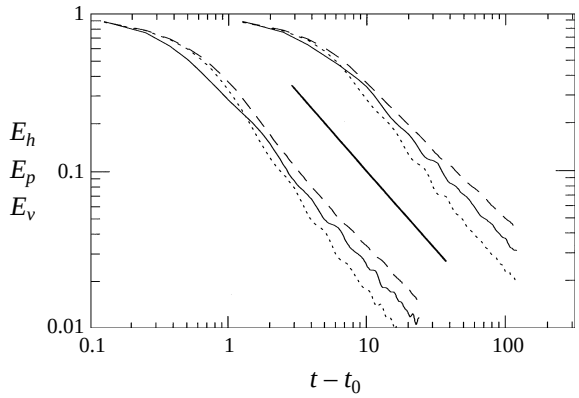

FIGURE 7. DNS results. Evolution as a function of dimensional time of; – – – –, the horizontal kinetic energy; ——, the potential energy; - - - -, the vertical kinetic energy. Left-hand set of curves: run R1; right-hand set of curves (shifted by one decade toward the right): run R2. All energies are normalized by their value at the time to stratification is added. A straight line of slope -1 is shown in between the two sets.

To compare the relative decay of the energy components displayed in figure 6, we have normalized these energies by their value at $t = t_0$ and plotted them versus dimensional time t. Results are displayed in figure 7 for the DNS R1 and R2. The potential energy decays sooner than the kinetic energy components in both runs for $t \leqslant 1$ while the vertical kinetic energy does not increase: no buoyancy effect is thus involved in this behaviour. Rather, strong nonlinear transfers of potential energy (relative to those of kinetic energy) occur toward small scales during this early stage. This results in an imbalance between the kinetic energy of the wave Φ_W and its potential energy E_p, which drives a non-zero and positive heat flux. The heat flux and normalized heat flux are plotted in figure 10 for run R1 and R2 (these curves are commented on in the next section). Figure 7 also shows that the relative decay of potential energy is stronger for run R1 than for run R2 because nonlinear interactions are stronger in the former run than in the latter, N being smaller. Hence the normalized heat flux should be stronger for the former run than for the latter. Figure 10(*c*) shows that this is indeed the case. This physical process very likely accounts for the larger-amplitude oscillations in Φ_W and E_p observed in run R1 compared to run R2 (see figure 6). Of course, it does not explain why the amplitude of the oscillations is overestimated by the EDQNM$_2$ model compared to the DNS results.

The stronger transfers of potential energy toward small scales occur during about half a Brunt–Väisälä period at the beginning of the simulations. Figure 10(*a*) shows that a strong positive heat flux occurs during this time: vertical kinetic energy is converted into potential energy to make up for the loss of potential energy by nonlinear transfers. Consequently, in figure 7, the vertical kinetic energy initiates a steeper decrease than the horizontal kinetic energy. This decay remains steeper than that of the potential energy, instead of oscillating about the same mean value, very likely because of the higher amount of potential energy at $t = t_0$ (we recall that all curves are normalized to 1 at $t = t_0$). The normalized heat flux does not exceed a few percent next (see figure 10*c*), so that the decay of the three curves is controlled by nonlinear transfers toward small scales. A clear hierarchy in these decay rates appears in figure 7, E_h decaying less than E_p, and E_p less than E_v. From about $2T_{BV}$, these

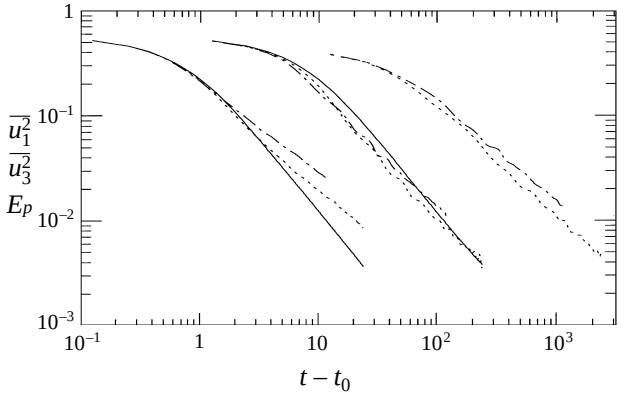

FIGURE 8. DNS results. Evolution as a function of dimensional time for: ——, run R0; - - - -, run R1; – – –, run R2. Left-hand set of curves: variance of the horizontal velocity, $\overline{u_1^2}$; middle set (shifted by one decade toward the right): variance of the vertical velocity, $\overline{u_3^2}$; right-hand set (shifted by two decades toward the right): potential energy E_p.

decay rates follow power laws with exponents close to -1, ranging between -1.1, for the vertical kinetic energy of run R1, to -0.86, for the horizontal energy of run R2.

The horizontal kinetic energy E_h ($\simeq \overline{u_1^2}$), twice the vertical kinetic energy ($\overline{u_3^2}$) and the potential energy are plotted versus time in figure 8 for runs R1, R2 and R0 (except for the potential energy for the latter run). At $t = t_0$, $\overline{u_1^2}$ and $\overline{u_3^2}$ are the volume-averaged variance of velocity components of an isotropic flow and are thus equal.

The behaviour of $\overline{u_3^2}$ for the stratified DNS results from both nonlinear transfers toward small scales and linear transfers into potential energy, as just said. In the early stage of the flow, figure 8 shows that $\overline{u_3^2}$ quickly departs from the isotropic curve, due to potential energy conversion, but the decay rate is about the same as for the isotropic DNS. Thus, buoyancy affects only the largest scale of the flow during that early stage. The inhibiting effect of buoyancy on nonlinear transfers (which involve intermediate and small scales) becomes visible from about $2T_{BV}$ for runs R1 and R2: the decay rate of $\overline{u_3^2}$ reduces from this time on. At the end of each DNS, the energy level has just exceeded that of the isotropic DNS.

Investigating the behaviour of $\overline{u_1^2}$, we note that the R1 and R2 curves depart from the R0 curve later in time than for $\overline{u_3^2}$, from $0.7T_{BV}$. The evolution of $\overline{u_1^2}$ up to this time seems to be decorrelated from that of $\overline{u_3^2}$: apart from an imperceptible and very temporary decrease of $\overline{u_1^2}$ below the R0 curve, there is no sign of the striking behaviour of $\overline{u_3^2}$ and of the potential energy. The same remark is made by LVA (p. 83) from their experimental results. From $0.7T_{BV}$, the decay rates of $\overline{u_1^2}$ become strongly dependent upon the value of N however, much more than for $\overline{u_3^2}$. Because 70% of E_h is contributed by the vortex mode, this suggests that another mechanism is responsible for the inhibition of energy transfer toward small scales: as already noted by previous authors, the vortex mode may be associated with two-dimensional motions transferring their energy predominantly toward large scales. 'Two-dimensional motions' should be understood here as motions lying more or less on isopycnal surfaces but depending upon the vertical direction, along which they are weakly correlated.

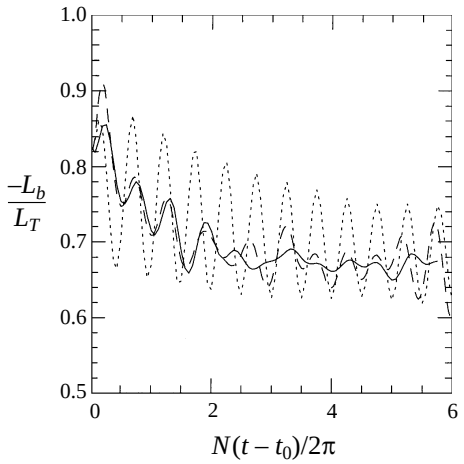

FIGURE 9. Time evolution of the ratio L_b/L_T. ——, DNS of run R1; – – – –, DNS of run R2; - - - -, EDQNM$_2$ model for run R2.

The experimental results of LVA and YW, obtained over $\simeq 0.8T_{BV}$, display the same features as ours. The temporal evolution of $\overline{u_1^2}$ for four different values of N remains close to the isotropic behaviour (with a lesser decay in YW experiments) while a strong scattering of the $\overline{u_3^2}$ curves, with slope steeper than the isotropic behaviour, is obtained. In the most stable experiment of YW, $\overline{u_3^2}$ eventually increases because of a net counter-gradient heat flux. No such effect occurs in our DNS.

5.3. *Overturning and buoyancy length scales*

The ratio of the vertical kinetic energy to the potential energy can be expressed as the square of the ratio of two length scales: the buoyancy length scale defined by equation (31) and an overturning length scale

$$L_T = (\overline{T^2})^{1/2}/N^2. \tag{38}$$

These scales are commonly used in laboratory experiments to characterize the flow dynamics. In the grid turbulence experiments of YW and LVA, the ratio L_b/L_T is always greater than 1, starting from a value of order 10 (depending upon the initial Froude number) and decaying smoothly toward 1. This is because the vertical kinetic energy is always greater than the potential energy. Our initial condition imposes a quite different behaviour on this ratio (figure 9): L_b/L_T remains smaller than 1 always, starting from a value of $\sqrt{2/3}$ (see relation (37)) and decreasing by 20% over the whole duration of the runs. This decrease attests that more vertical kinetic energy is converted into potential energy than potential energy into kinetic energy, as already noted. A constant mean level close to $2/3$ seems to be reached from about $1.5T_{BV}$. The EDQNM$_2$ model catches quite well the mean behaviour observed for L_b/L_T, apart from an overestimation of the amplitude of the oscillations.

Recent analytical results using RDT by Hanazaki & Hunt (1996) have also predicted that L_b/L_T should reach an asymptotic value, at infinite time, but equal to $\sqrt{2/3}$. This result, as all of those obtained by Hanazaki & Hunt (1996), is based upon the assumption that the velocity and temperature fluctuations have isotropic spectra. While this is the case in our calculations at $t = t_0$, we have shown that the RDT is not able to predict the flow behaviour, our initial condition being designed so as to

minimize linear effects. Moreover, due to our choice of the potential energy at $t = t_0$, L_b/L_T starts from the asymptotic value $\sqrt{2/3}$ predicted by the RDT. We still note that the final value reached by this ratio in our calculations is lower by only 20% than the RDT prediction.

5.4. *Heat flux*

The volume-averaged heat flux computed by the DNS and by the EDQNM$_2$ model is plotted in figure 10(*a*) for run R2. Note that $-\overline{u_3 T}$ is plotted. The heat flux first decreases down to zero during $0.1T_{BV}$ and becomes slightly counter gradient, very likely because the potential energy is 1.5 larger at $t = t_0$ than the vertical kinetic energy. The heat flux dramatically increases next, signalling that the transfers of potential energy toward small scales have been initiated: large-scale vertical kinetic energy is converted into potential energy. At about $0.5T_{BV}$, rising fluid particles do not have enough kinetic energy to continue their ascent and fall back toward their equilibrium position, leading to a (weakly) negative counter-gradient flux. The amplitude of the oscillations drops from about $2T_{BV}$: the vertical scales of the flow collapse from this time on (this event will be confirmed by subsequent analysis of the flow). Note that the net heat flux over the whole simulation is down gradient.

The normalized heat flux (correlation coefficient between the vertical velocity and the temperature fluctuation) is plotted in figure 10(*b*). Its value is close to 0 at $t = t_0$ because the vertical velocity and temperature field are decorrelated at that time (through the random realization of the temperature phases). Its maximal absolute amplitude is about one order of magnitude smaller than in wind tunnel experiments (of order 0.7 in the latter case, the temperature first behaving as a passive scalar). Unlike laboratory experiments also, the amplitude of the oscillations stays about the same as time elapses, being equal to a few times 0.01 (it falls below 0.03 after $2T_{BV}$). As stated above, we designed our initial condition so as to minimize this correlation coefficient. This coefficient displays oscillations at a well-defined frequency, nearly equal to $2N$. This result has been predicted rigorously from RDT by Hanazaki & Hunt (1996, equation (4.47)). According to equation (20), the heat flux is mostly contributed by large-scale motions (since the largest values of $\Psi(\boldsymbol{k})$ are reached at those scales), with which the wavevector makes an angle θ_k with vertical. The frequency of these motions being close to N, as just seen, they consist of large-scale internal waves that propagate almost horizontally. Note that the amplitude of the correlation coefficient varies in time, possibly because of interactions between these large-scale waves.

The EDQNM$_2$ model predicts rather well the behaviour of the heat flux (figure 10*a*). In particular, the frequency of the oscillations is the same as in the DNS (recall that no attention should be given to the relative phase of the oscillation). The amplitude of the oscillations is about correct though it decreases too regularly compared to the DNS behaviour. However, when the correlation coefficient is considered (figure 10*b*), the amplitude of the oscillations appears to be overpredicted by the model: from $2T_{BV}$, the maximum amplitude is three times too high. This indicates that the EDQNM$_2$ model does not proceed to a great enough decorrelation between the vertical velocity and the temperature fluctuation. However, the correlation coefficient is very small, less than 0.06, both in the DNS and in the EDQNM$_2$ model. It is very likely that, from a physical point of view, only this smallness matters and that the overestimation by the EDQNM$_2$ model is not dynamically significant.

The predictions of the heat flux and of the correlation coefficient by the RDT are also plotted in figures 10(*a*) and 10(*b*) respectively. Their values are nearly zero at

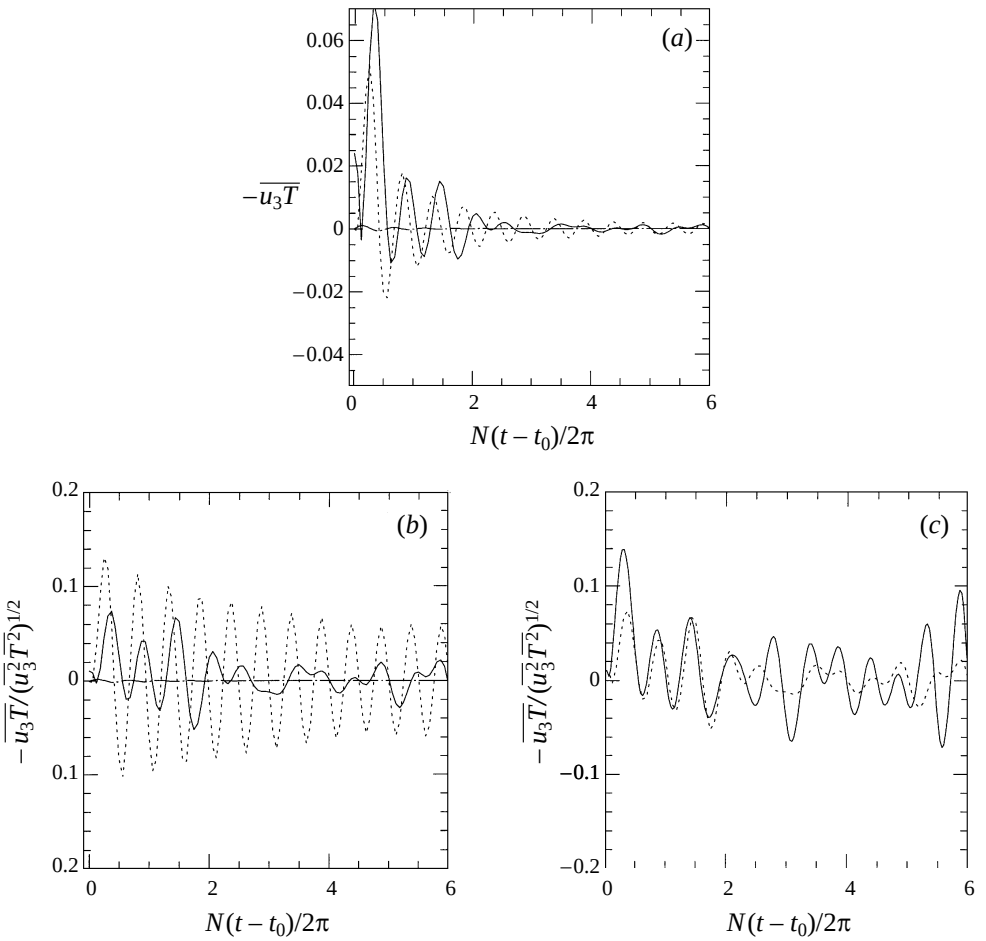

FIGURE 10. (*a*) Vertical heat flux for run R2 and (*b*) Normalized heat flux for run R2. ——, DNS; - - - -, EDQNM$_2$ model; – – –, RDT. (*c*) DNS results only: normalized heat flux. ——, run R1; - - - -, run R2.

any time, which confirms that nonlinear terms control the evolution of the large-scale flow in the DNS and in the EDQNM$_2$ model. Hence, the linear model does not predict correctly the flow behaviour.

5.5. *Similarity law for the vertical kinetic energy*

In LVA's paper, the vertical kinetic energy is plotted for experiments having different values of N (their figure 6) and a rather strong scattering appears when the curves are displayed as a function of real time. LVA were able to make the curves collapse on a single one by normalizing the vertical kinetic energy by its isotropic counterpart, to eliminate viscous effects (supposing cumulative viscous effects are the same in the isotropic and non-isotropic flows) and by plotting the normalized vertical kinetic energy against t/T_{BV} (their figure 7). The fact that a similarity law is obtained indicates that the vertical kinetic energy decay is driven by cumulated buoyancy effects.

We have applied the same normalization process to the vertical velocity of runs r1, r2, R1 and R2. The normalized vertical kinetic energies are plotted as a function

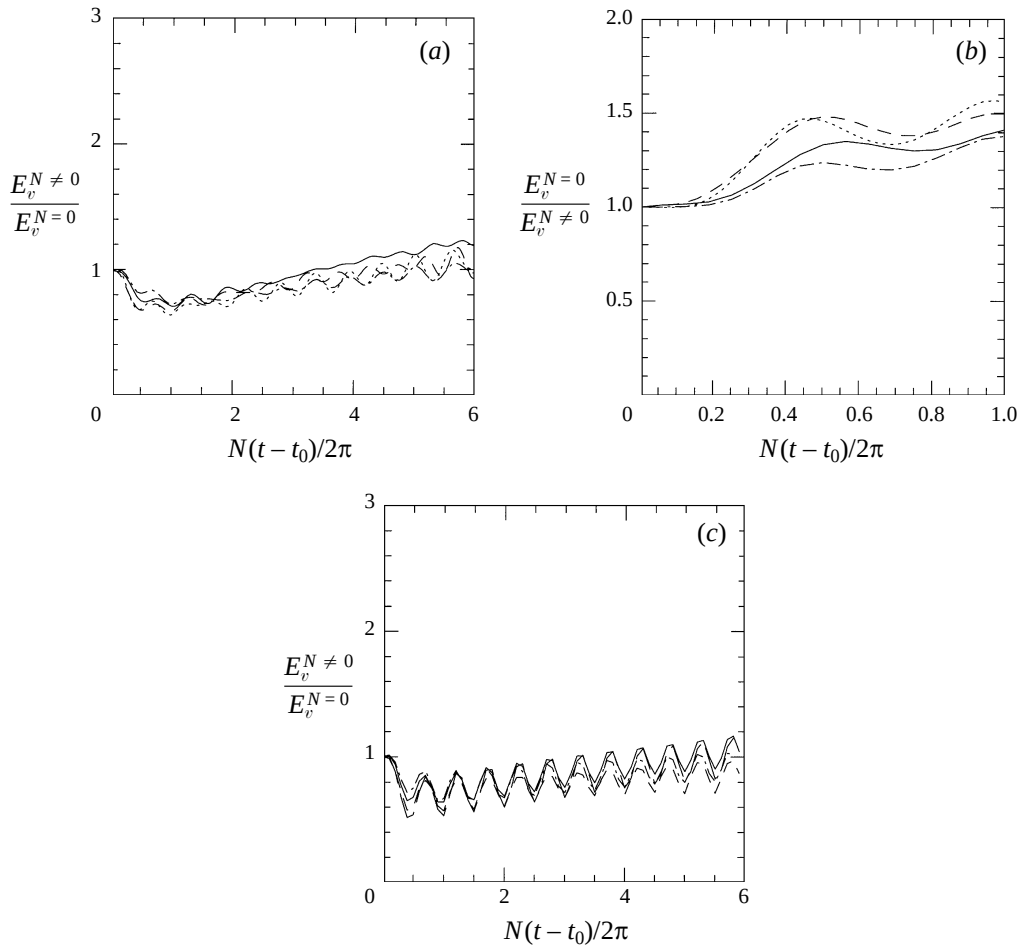

FIGURE 11. (*a*) DNS results. Vertical kinetic energy $E_v^{N\neq 0}$ for different stratified calculations, normalized by the instantaneous isotropic counterpart $E_v^{N=0}$, over $6T_{BV}$. ----, run r1; – – –, run r2; – – – –, run R1; —— run R2. (*b*) DNS. Same as (*a*) except that the inverse ratio $E_v^{N=0}/E_v^{N\neq 0}$ is plotted, over one Brunt–Väisälä period only. (*c*) Same as (*a*), but for the EDQNM_2 model.

of $(t-t_0)/T_{BV}$ on figure 11 (*a*): all curves collapse on a single one, at least up to $3T_{BV}$. As already shown in § 4.2, we ignore the phase difference in the oscillations, which is inherent in the random realization used to initiate deterministic velocity and temperature fields.

To compare this behaviour over the first Brunt–Väisälä period with LVA's result, we adopt the same representation as these authors. In figure 11 (*b*) is thus plotted the inverse of the normalized kinetic energy up to one Brunt–Väisälä period. We first note that the curves in figure 11 (*b*) display the same qualitative behaviour but differ in level. This indicates that the flow dynamics are not quite governed by buoyancy effects. The common behaviour displayed by all four curves is still analogous to LVA's result. Thus, as in the experiments, the vertical kinetic energy first decays at the unstratified rate during $0.1T_{BV}$ (passive behaviour); the curves next increase and reach a maximum value at about $0.5T_{BV}$. This maximum value corresponds to the maximum loss of vertical kinetic energy through conversion into potential energy. This loss amounts to at most 30% of the initial vertical kinetic energy. In

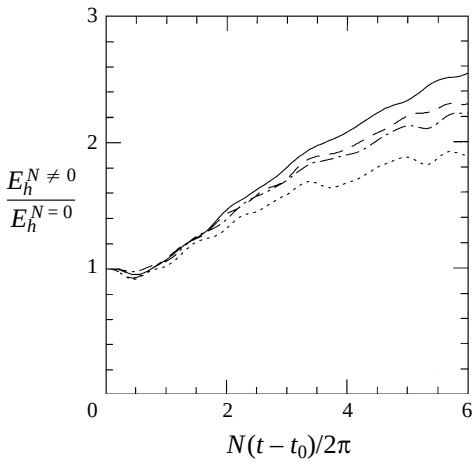

FIGURE 12. DNS results. Horizontal kinetic energy $E_h^{N\neq 0}$ normalized by its instantaneous isotropic counterpart $E_h^{N=0}$. ----, run r1; – –, run r2; – – – –, run R1; ——, run R2.

the experiment, it is equal to 60% of the vertical energy just behind the grid; there is very little potential energy in the initial grid turbulence and vertical kinetic energy provides the only source of potential energy. In our situation, a large reservoir of potential energy is available. These results show that, in our case, nonlinear transfers of potential energy toward small scales drive a rather strong loss of vertical kinetic energy. In the experiment of LVA as well as in figure 11 (*b*), the curves next slightly decay and reach a plateau: the vertical kinetic energy decays again at the unstratified rate, but has a lower value than at $t = t_0$ (its normalized value is equal to $\simeq 1.35$ in the present case and to 2 in the most stable run of LVA's experiments). LVA next observed an increase of the similarity function for their most stable run, which they relate to the presence of active buoyancy forces at all scales of motions. Figure 11 (*a*) shows that this is indeed the case: the plateau is followed by an increase of the curves. More precisely, the plateau extends more or less up to $\simeq 1.5T_{BV}$, that is, up to the time the vertical scales collapse. The rate of decrease of the vertical kinetic energy is reduced from this time on, leading to an increase of the curves in figure 11 (*a*).

The same normalization process has been applied to the vertical kinetic energy calculated by the EDQNM$_2$ model. The initial stage until one Brunt–Väisälä period is not very well reproduced by the model, mainly because the amplitude of the oscillations is overestimated by the model, which hides this earlier behaviour (figure 11 *c*). From one Brunt–Väisälä period however, the EDQNM$_2$ model reproduces closely the similarity law stemming from the DNS.

It follows that, from one Brunt–Väisälä period, the vertical kinetic energy can be easily modelled. From figures 11 (*a*) and 11 (*c*), one gets

$$\frac{E_v^{N\neq 0}(t)}{E_v^{N=0}(t)} = 0.09 \left(\frac{N}{2\pi}(t-t_0) + 6.9\right). \tag{39}$$

Since the unstratified vertical kinetic energy in our DNS behaves as $E_v^{N=0}(t) = 0.6\ t^{-1.38}$, the vertical kinetic energy for the stratified runs can be modelled as

$$E_v^{N\neq 0}(t) = 0.054\ t^{-1.38} \left(\frac{N}{2\pi}(t-t_0) + 6.9\right). \tag{40}$$

The same normalization process has been applied to the horizontal kinetic energy (figure 12). Three stages can be distinguished. The horizontal kinetic energy decays at the isotropic rate up to $0.7T_{BV}$, as we already noted from figure 8 (we still observe that, for runs r1 and R1, E_h decays slightly more than the isotropic rate: some transfers into vertical kinetic energy by pressure–velocity correlation should occur). From $0.7T_{BV}$, the decay rate of E_h starts to decrease, compared to the isotropic decay, signalling some influence of buoyancy effects. The normalization of the data shows that, apart from viscous effects, the decrease of the horizontal kinetic energy is accounted for by the cumulated effect of buoyancy effects, up to $2T_{BV}$: the four curves remain close up to this time. These four curves start to separate next, and E_h eventually reaches values up to 2.5 greater than the isotropic level. This is in contrast to the behaviour of the vertical kinetic energy, which hardly exceeds the isotropic value after $6T_{BV}$. This indicates that both energies are associated with distinct scales, small ones for E_v and large ones for E_h. Figure 12 thus shows that the large-scale horizontal vortex motion starts emerging from turbulence from $2T_{BV}$.

5.6. *Dissipation rate of the kinetic energy*

The dissipation rate of kinetic energy is plotted versus dimensional time (t) in figure 13 (*a*) for runs R0, R1 and R2. All three quantities follow the same isotropic law up to $t \simeq 1$. The stratified dissipation rates next decrease more strongly than the isotropic dissipation rate and thus depart from the R0 curve: the nonlinear transfer of potential energy toward small scales indirectly accounts for this behaviour, in depleting the kinetic energy reservoir at large scales. Both stratified dissipation rates next again follow the isotropic decay rate, indicating that the smallest scales of the flow are not affected yet by stratification. A sudden change in these decay rates occurs for run R2 at $t-t_0 = 3$, i.e. at $1.5T_{BV}$, and for run R1 at $t-t_0 = 6$, i.e. at $1.5T_{BV}$ also. Hence, the collapse of the vertical scales that occurs at that time very likely results in all scales of motions, up to the smallest ones, being influenced by buoyancy. Both stratified dissipation rates eventually become larger than the isotropic one.

The fact that the stratified dissipation rates become driven by buoyancy after the collapse invites one to employ the same normalization as in the previous section. This is done in figure 13 (*b*), for runs r1, r2, R1 and R2. The scenario just described from figure 13 (*a*) is successively manifested in figure 13 (*b*) as (i) a constant initial level, during a very short time; (ii) a decrease of the curves, which shows that the loss of vertical kinetic energy through conversion into potential energy leads to a 20% to 30% lower value of the stratified dissipation rate compared to the isotropic case; (iii) and a plateau, up to $1.5T_{BV}$. An analogous behaviour can be inferred from figure 9 of LVA (up to $0.8T_{BV}$), the stratified dissipation rate for their most stable experiment reaching a value 60% lower than the isotropic value however. Coming back to figure 13 (*b*), we note that the four curves increase from about $2T_{BV}$ and closely follow a common law. The corresponding similarity function can be easily modelled:

$$\frac{\epsilon^{N\neq 0}(t)}{\epsilon^{N=0}(t)} = 0.163\left(\frac{N}{2\pi}(t-t_0)+2.92\right) \qquad \text{with} \qquad \epsilon^{N=0}(t) = 0.44(t-0.55)^{-2.3}. \quad (41)$$

Equation (41) shows that $\epsilon^{N\neq 0}$ increases with N at large times, which we found in figure 13 (*a*).

It is of interest to compare the dissipation rate $\epsilon_{N\neq 0}$ to the volume-averaged heat flux $\overline{u_3 T}$. The ratio of these two quantities is a common measure of instantaneous

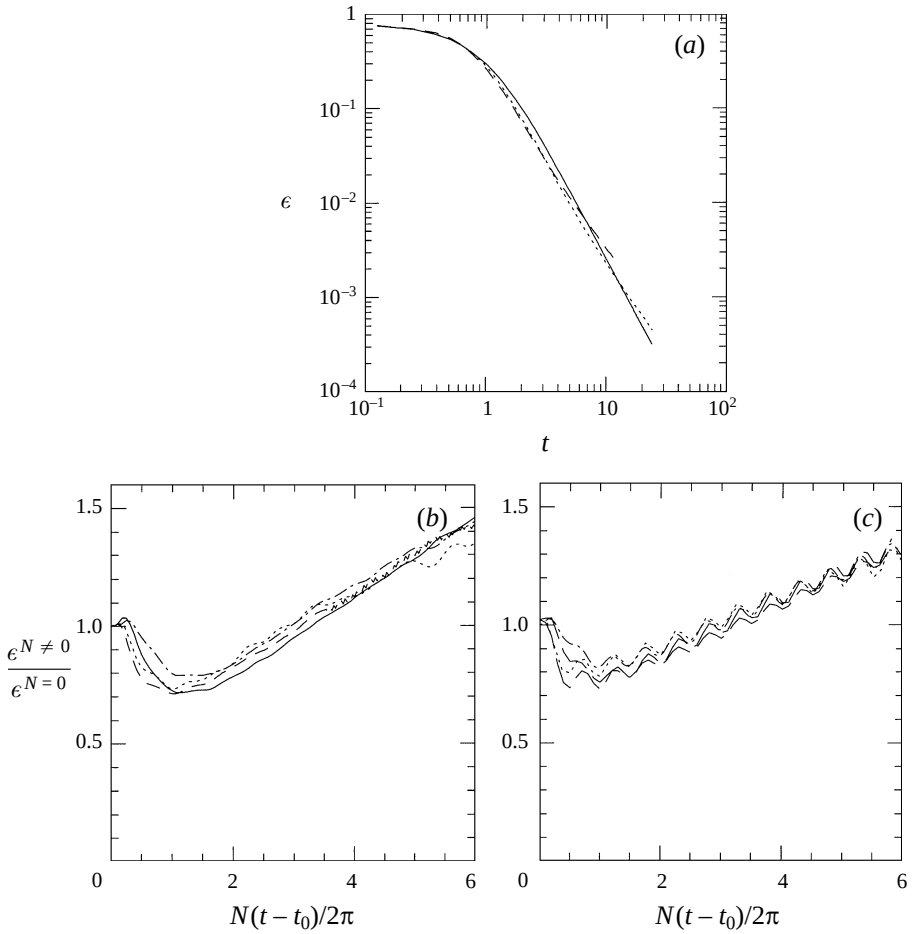

FIGURE 13. (*a*) DNS results. Dissipation rate of kinetic energy as a function of dimensional time t. ——, run R0; - - - -, run R1; – – – –, run R2. (*b*) DNS results. Dissipation rate of kinetic energy $\epsilon^{N\neq 0}$ normalized by its instantaneous isotropic counterpart $\epsilon^{N=0}$ as a function of the non-dimensional time $(t-t_0)/T_{BV}$. - - - -, run r1; – – –, run r2; – – – –, run R1; ——, run R2. (*c*) Same as (*b*) but for the EDQNM_2 model.

mixing efficiency used by oceanographers. (Mixing efficiency is defined by the rate at which potential energy is produced by a given amount of kinetic energy E_k, through the lifting of cold fluid particles for instance, relative to the rate at which E_k is dissipated. Note that this definition assumes that all of the potential energy produced is used for fluid mixing.)

In figure 14 $\overline{u_3 T}/\epsilon$ is plotted (with a minus sign) as a function of $(t-t_0)/T_{BV}$ for runs R1 and R2. The EDQNM_2 prediction is also plotted for the latter run. All three curves display precisely the same behaviour over the first Brunt–Väisälä period: they start from zero, reach a first maximum value of 0.16 at $\simeq 0.3T_{BV}$, a slightly negative minimum value at $0.6T_{BV}$ before increasing again. Interestingly, this behaviour coincides with that obtained by LVA (their figure 10) and by YW (their figure 26). It is noteworthy that this behaviour is quantitatively obtained in three situations which differ in the initial condition, whereas stratified flows dynamics usually strongly depend upon the initial condition. We also note that the maximum

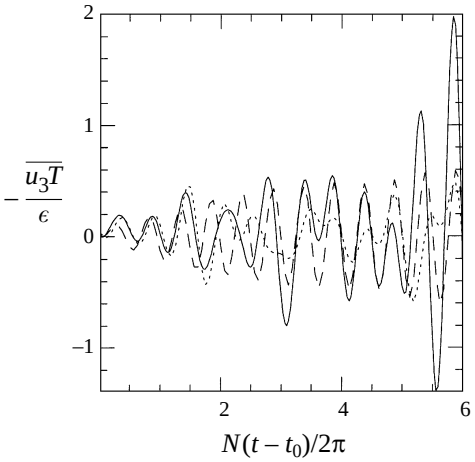

FIGURE 14. Ratio of vertical heat flux to dissipation rate of kinetic energy. ——, DNS of run R1; - - - -, DNS of run R2; – – – –, EDQNM$_2$ model for run R2.

value of 0.16, curiously, is very close to the mixing efficiency measured in the oceanic thermocline ($\simeq 0.2$) from ensemble averages.

5.7. *Energy in the Craya–Herring modes*

In this subsection, we investigate the temporal behaviour of the volume-averaged kinetic energy of the vortex and wave parts of the flow, which we compare to the volume-averaged potential energy. This permits the analysis of the energetics of the flow initiated in the previous subsections to be complemented.

Recall that the vortex part is solely horizontal; thus, the horizontal kinetic energy $E_h(t)$ contains all of its energy $\Phi_V(t)$, plus the horizontal component of the kinetic energy of the wave part. At $t = t_0$, 75% of E_h is contributed by the vortex part; this contribution slightly decreases and reaches a constant ratio from one Brunt–Väisälä period, equal to 70% for runs R1 and R2 (as already noted in § 5.2). The vertical component of the wave kinetic energy is the vertical kinetic energy of the flow.

$\Phi_V(t)$, $\Phi_W(t)$ and $E_p(t)$ are plotted in figures 15(*a*) (DNS results) and 15(*b*) (EDQNM$_2$ results) for run R2. The interest of the Craya–Herring decomposition appears in this figure: the kinetic and potential energy of the wave part now oscillate about the same mean level, with opposite phases, as expected from a wave motion. We have shown in figure 6 that the decay rate of potential energy is well predicted by the EDQNM$_2$ model. Thus, the decay rate of Φ_W is well predicted also since it behaves identically to E_p in figures 15(*a*) and 15(*b*). The striking feature of figure 15 is the behaviour of Φ_V. First, it does not display any visible oscillation. This implies that the mathematical Craya–Herring decomposition into wave and vortex parts has a physical relevance in the present case. This also implies that no interactions, or very weak ones, occur between the wave and the vortex parts of the flow. The same remark has also been made by Métais & Herring (1989) from their 64^3 direct numerical simulations. Using perturbation methods, Lelong & Riley (1991) did not find any such interactions at lowest order in the expansions of the velocity and temperature fields, the Froude number being the small parameter. Secondly, figure 15 shows that the decay rate of the vortex part is slower than that of the wave part, leading to

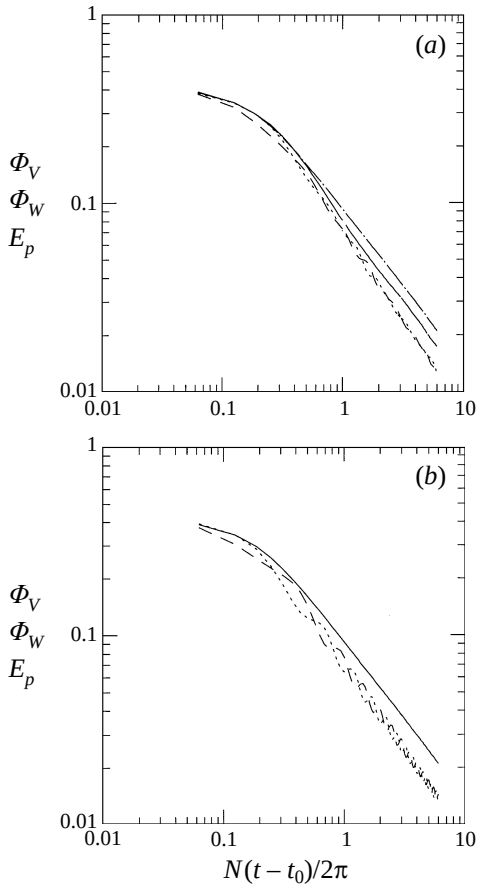

FIGURE 15. Energy in the Craya–Herring modes for run R2: ——, vortex kinetic energy Φ_V; - - - -, wave kinetic energy Φ_W; – – – –, potential energy E_p. (*a*) DNS results; for comparison, the upper curve – - – reproduces Φ_V predicted by the EDQNM$_2$ model. (*b*) EDQNM$_2$ model.

an energetic domination of the vortex mode. This is consistent with this mode having a quasi-two-dimensional dynamics, as already noted. Figure 15(*b*) shows that the EDQNM$_2$ model predicts the same behaviour for the vortex part, except for an even slower decay rate. Thus the EDQNM$_2$ value differs by 14% from the DNS value at $6T_{BV}$. This discrepancy between EDQNM$_2$ and DNS in the vortex part accounts for the discrepancies we have pointed out in previous sections – in the comparison of the Reynolds number plotted in figure 4(*a*), of the total energy plotted in figure 5(*c*) or the horizontal kinetic energy plotted in figure 6 – because the horizontal velocity component comes into play in these quantities.

To check whether a confinement effect in the DNS is responsible for this discrepancy, we should carry out a simulation analogous to run R2 except that the domain side, and thus the resolution, would be doubled. This checking becomes possible if applied to a 128^3 DNS such as run r2. We have thus run a DNS of resolution 256^3 with domain side 8π (run R4 in table 1), the physical parameters being identical to those of run r2. We have found (not shown) that the vortex kinetic energy differs by less than 1.5% between the two runs over 6 Brunt–Väisälä periods. Hence, no

confinement effect occurs in run r2. Since confinement concerns scales that are the least sensitive to the viscosity, we conclude that the same result can be applied to run R2.

5.8. *Energy density spectra of the Craya–Herring modes*

5.8.1. *DNS results*

The kinetic energy density spectrum of the vortex part, $\Phi_1(k,t)$, and of the wave part, $\Phi_2(k,t)$ and the potential energy density spectrum $\Phi_3(k,t)$, are superposed in figure 16 for run R2. These spectra are spherically averaged for comparison purpose with the EDQNM$_2$ results. Each spectrum results from an average over one Brunt–Väisälä period (except when plotted at $t = t_0$). At $t = t_0$, all three spectra coincide for scales smaller than the scale at which the spectra peak. Some differences can be noted in the largest scales (figure 16 *a*), which are simply due to the scarcity of modes in the spherical shells over which the spectra are averaged. The spectra averaged over the first Brunt–Väisälä period are also displayed in figure 16 (*a*). Two major features can be noted. One is related to the level of the potential energy, which is lowest at intermediate scales but highest at small scales. This behaviour is a clear manifestation of the strong transfer of potential energy toward small scales in the very early stage of the flow. The second feature is related to the level of the vortex energy spectrum, which is opposite to that of the potential energy spectrum: the vortex part dominates at large scales and its energy at small scales starts to separate from the wave kinetic energy. An inspection of these three superposed spectra at successive times during the first Brunt–Väisälä period reveals that the strong potential energy transfers first set in, at an inertial time earlier than $t-t_0 = 1$. The reduction in the transfer rates within the vortex part follows, but on a buoyancy time scale: the vortex spectrum start to differ at all scales from the wave kinetic energy spectrum from $\simeq 0.5T_{BV}$ in runs R1 and R2.

The strong transfer rates of potential energy toward small scales are quickly weakened by the stable stratification, as already seen, and from two Brunt–Väisälä periods, the potential energy spectrum almost matches that of the wave kinetic energy. By contrast, the vortex part kinetic energy remains distinct from the wave part kinetic energy at all scales, both spectra crossing at $k/k_{min} \simeq 10-15$ (figure 16 *b*, left-hand set of curves). The fact that the vortex part involves larger scales than the wave part is demonstrated when viscous effects are increased, because viscous effects have less damping action on large scales than on the small ones. Thus, in run r1 where the viscosity is twice as large as in run R1, the vortex part clearly dominates the largest scales of the flow, up to one tenth of the box side (figure 16 *b*, middle set of curves). (The latter effect was also noted in the lower resolution–and thus higher viscosity – DNS of Métais & Herring 1989.) A higher stratification level also promotes the large-scale dominance of the vortex mode (figure 16 *b*, right set of curves). As time elapses, stratification effects gain importance over nonlinear effects and so also do viscous effects (the flow being unforced). It follows that, over a long time, the vortex part should energetically dominate the large scales of the flow in run R1 and, more generally, in any stratified simulation.

5.8.2. *Comparison with the* EDQNM$_2$ *model.*

Instead of presenting the spectra for the EDQNM$_2$ model as in figure 16, we think it more useful to present a comparison of instantaneous spectra of the vortex and wave parts between the EDQNM$_2$ model and the DNS, at successive times $(t-t_0)/T_{BV} = 0, 1, 3$ and 6. Results are presented in figure 17 for run R1 but are

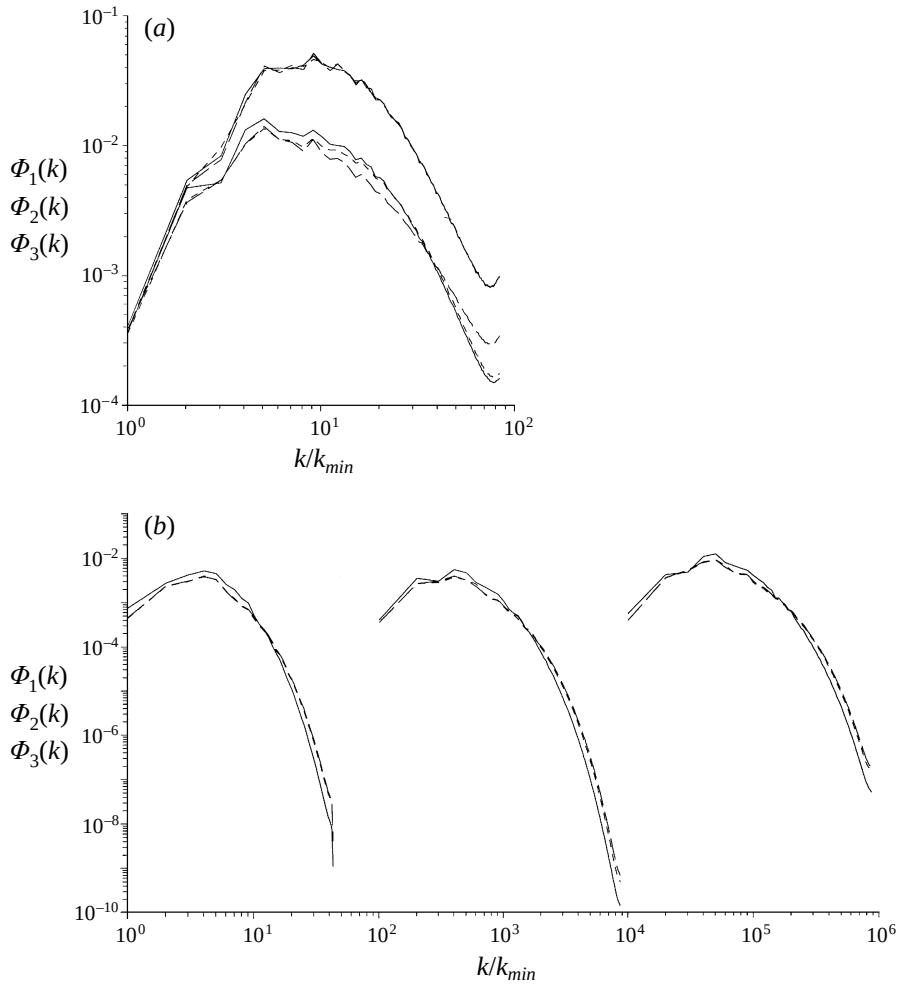

FIGURE 16. DNS results. Spherically averaged energy density spectra of the Craya–Herring modes as a function of k/k_{min} with $k_{min} = 1/2$: ——, vortex kinetic energy spectrum $\Phi_1(k)$; - - - -, wave kinetic energy spectrum $\Phi_2(k)$; – – – –, potential energy spectrum $\Phi_3(k)$. (*a*) Run R1. Upper set of curves: spectra at $t = t_0$; lower set of curves: spectra averaged over the first Brunt–Väisälä period. (*b*) Spectra averaged over the third Brunt–Väisälä period. Left-hand set of curves: run r1; middle set (shifted by two decades toward the right): run R1; right-hand set (shifted by four decades toward the right): run R2.

similar for run R2. The large-scale behaviour of the wave part spectra, $\Phi_2(k)$ and $\Phi_3(k)$, cannot be compared precisely because the spectra oscillate at these scales and there are phase differences between the EDQNM$_2$ predictions and the DNS data. In the small scales, the spectra match rather well. Regarding the vortex part spectra, the smallest scales predicted by EDQNM$_2$ are less energetic than those computed by the DNS. This suggests that transfers within the vortex part toward small scales are too strongly reduced in the EDQNM$_2$ model. This would account for the higher kinetic energy level at large scales (for $k/k_{min} \geqslant 3$) predicted by the EDQNM$_2$ model, supposing transfers with the wave part kinetic energy are correctly modelled (these transfers may however be extremely weak). This result also accounts for the overprediction of the vortex part kinetic energy in figure 15.

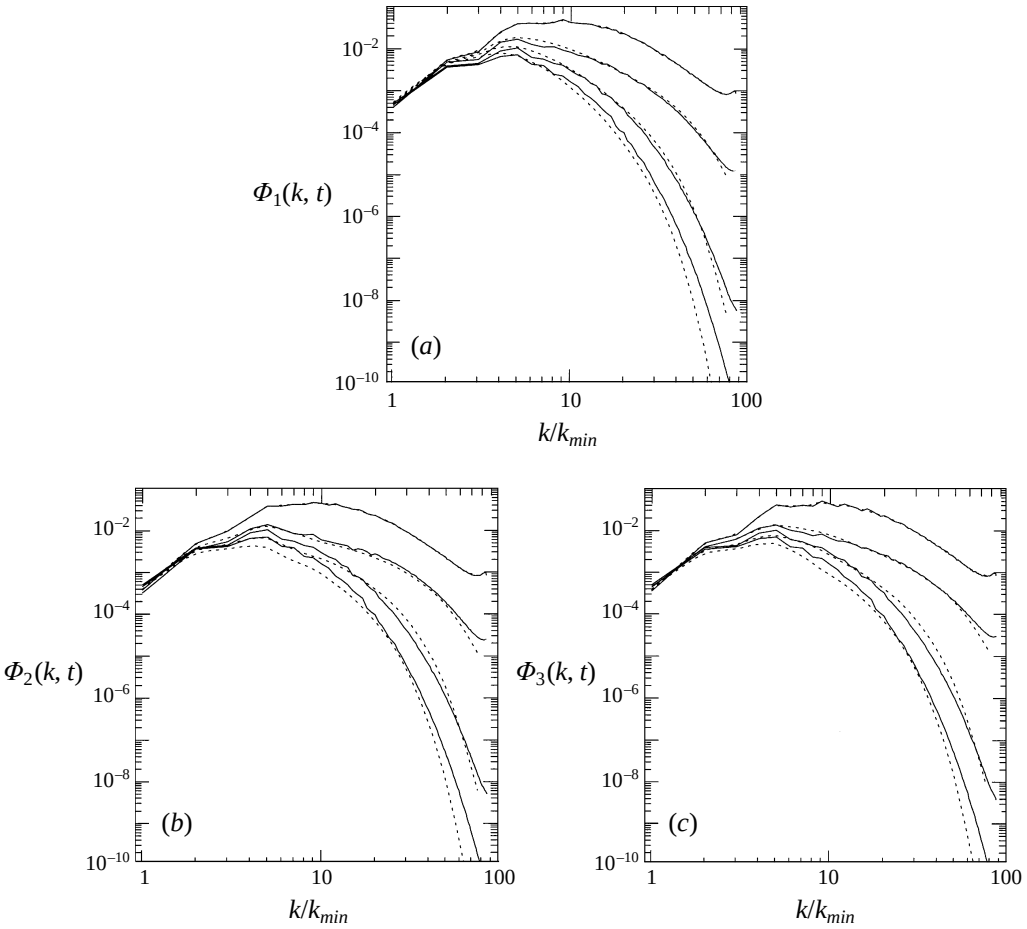

FIGURE 17. Instantaneous spherically averaged energy density spectra of the Craya–Herring modes as a function of k/k_{min} with $k_{min} = 1/2$, for run R1. ——, DNS; - - - -, EDQNM$_2$ model. Upper curve: $t = 0$; upper middle curve: $t/T_{BV} = 1$; lower middle curve: $t/T_{BV} = 3$; lower curve: $t/T_{BV} = 6$. (*a*) Vortex kinetic energy spectrum; (*b*) wave kinetic energy spectrum; (*c*) potential energy spectrum.

5.9. *Heat flux spectra*

5.9.1. *DNS results*

The transfers of potential energy toward small scales invite one to study the heat flux spectrum. The heat flux spectrum is computed as the real part of the correlation $\hat{u}_3^*(\boldsymbol{k})\hat{T}(\boldsymbol{k})$, averaged over spherical shells to permit comparison with the EDQNM$_2$ model. We have checked however that the same qualitative wavenumber dependence is obtained whether this spectrum is computed as a function of the vertical wavenumber or the horizontal wavenumber. The spherically averaged heat flux spectrum is referred to as $F(k)$ in the following. A negative value of $F(k)$ means that temperature variance is produced at the expense of kinetic energy at scale k. Physically, cold (resp. hot) fluid is displaced upwards (resp. downwards) from its equilibrium position. By contrast, a positive value of $F(k)$ corresponds to a counter-gradient flux: kinetic energy at scale k is produced at the expense of potential energy. This is the case when fluid particles go back toward their equilibrium position. The fluid 're-stratifies' then, as it is sometimes expressed.

The heat flux spectrum averaged over the first Brunt–Väisälä period for run r1 is plotted in figure 18 (*a*): $kF(k)$ is plotted as a function of $\log(k)$, as has become usual, to highlight the small-scale behaviour while getting the net heat flux from the algebraic sum of positive and negative areas. Note that $-kF(k)$ is plotted. As already seen, the loss of potential energy at large scales due to nonlinear transfers toward small scales is partly made up by conversion of vertical kinetic energy at large scales. This leads to a down-gradient heat flux spectrum at the latter scales, that occurs from $t = t_0$ up to $(t-t_0)/T_{BV} \simeq 0.5$. The largest scales of the flow become dominantly counter-gradient next (figure 18 *b*) and reverse again at about $0.75T_{BV}$, while decreasing in amplitude. (The shape of the spectrum in figure 18 (*a*) is thus dominated by the contribution of the spectra during the first half-Brunt–Väisälä period.) This large-scale oscillatory behaviour is consistent with the temporal evolution of the volume-averaged heat flux plotted in figure 10. By contrast, a counter-gradient flux occurs at small scales, for $k/k_{min} > 20$, as a response of the excess of potential energy at those scales (relative to the equipartition with wave kinetic energy at $t = t_0$). This counter-gradient flux occurs very early, being already visible at $T_{BV}/16$. The fact that the minimum value in the counter-gradient part is located near the cut-off wavenumber in figures 10 (*a*) and 10 (*b*) possibly reflects an insufficient damping by viscosity. Indeed, the minimum value of the counter-gradient part moves toward smaller k during the second half of the first Brunt–Väisälä period and the spectral shape about this value smooths. Later in time, $F(k)$ averaged over each successive period displays oscillations about zero in the largest scales. By contrast, the spectrum is persistently counter gradient at small scales, but with an amplitude ten times smaller than the maximal amplitude of the large-scale oscillations. The range of scales at which $F(k)$ is counter gradient extends toward smaller wavenumbers over time (the wavenumber at which it vanishes decaying from 20 to 5, in units of k_{min}), indicating that the flow progressively relaminarizes.

To get a quantitative estimate of how important these fluxes are relative to the level of the kinetic and potential energy spectra, we have normalized $F(k)$ by the square root of the vertical velocity spectrum times the temperature fluctuation spectrum. Each spectrum is spherically averaged and temporally averaged over the first Brunt–Väisälä period prior to normalization. The normalized heat flux spectrum thus obtained is plotted in figure 18 (*c*). It reaches values up to 10 % in the largest scales and 14 % (in absolute value) in the smallest scales. Hence, at no scales does the heat flux significantly influence the flow dynamics. In this sense, the (spherically averaged) heat flux can be said to be weak at all scales. Regarding the smallest scales, the 14 % contribution (at most) explains why the dissipation rate decays at the same rate as its isotropic counterpart during the first Brunt–Väisälä period. By contrast, we have found that, during the second Brunt–Väisälä period, the normalized heat flux reaches 40 % (in absolute value) at small scales; this is in agreement also with figure 13 (*a*), which shows that the dissipation rate is influenced by buoyancy effects from $\simeq 1.5T_{BV}$.

The oscillation about zero of the heat flux spectrum at large scales in strongly stratified flows has already been mentioned by several authors (e.g. Gerz & Schumann 1991; Gerz & Yamazaki 1993), for different Prandtl numbers and for initial conditions of either no (or little) potential energy or no kinetic energy. The existence of a persistent counter-gradient heat flux at small scales is also a feature of stratified flows and the role of the molecular Prandtl number and of the Reynolds number upon this flux is discussed in Gerz & Schumann (1991, 1996) or Komori & Nagata (1996) for instance.

In LVA's and YW's experiments, only a very weak counter-gradient flux, relative to the level of the flux at large scales, can be detected. This weakness has been

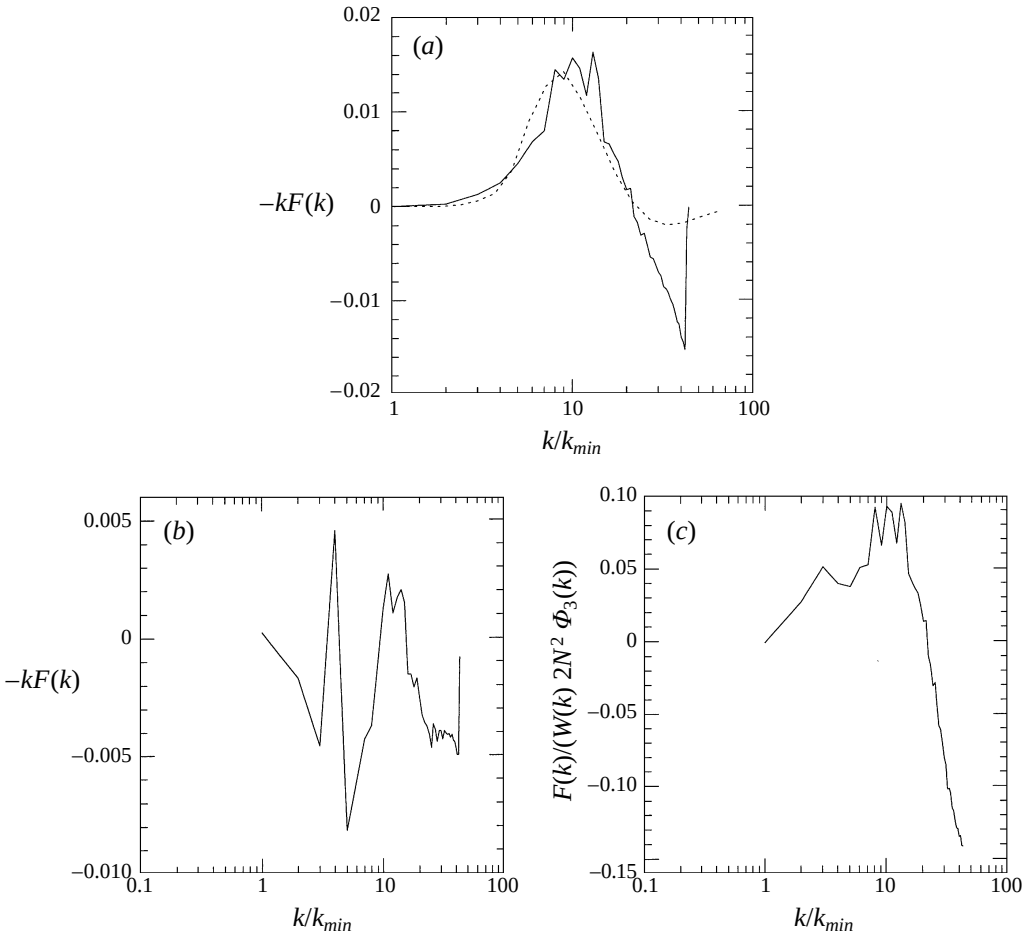

FIGURE 18. (*a*) Vertical heat flux spectrum $F(k)$ for run r1 as a function of k/k_{min}. $F(k)$ is averaged over spherical shells of radius k and over the first Brunt–Väisälä period: ——, DNS results; ----, $EDQNM_2$ model. (*b*) DNS results for run r1. Instantaneous vertical heat flux spectrum, at $N(t-t_0)/2\pi = 0.56$. (*c*) DNS results for run r1. The vertical heat flux spectrum is normalized by the square root of the spectrum of the vertical velocity, $W(k)$ times the spectrum of the temperature fluctuation, $2\,N^2\Phi_3(k)$. All three spectra are spherically averaged and temporally averaged over one Brunt–Väisälä period prior to normalization.

attributed by previous authors to the Prandtl number (equal to 0.7) being smaller than 1, because temperature fluctuations are diffused faster at small scales than velocity fluctuations. We have found that, during the first Brunt–Väisälä period, the buoyancy flux has no dynamical influence on the small-scale behaviour, as in LVA's experiments. A difference with these experiments however concerns the instant at which this counter-gradient heat flux sets in. In the calculations reported in the present paper, it occurs nearly from the beginning of the stratified flow evolution. By contrast, it develops from $\simeq 0.5T_{BV}$ in LVA's and YW's laboratory experiments. To check the dependence of this time upon the initial condition, we have performed two direct numerical simulations for $N = \pi$ and $N = \pi/2$, with no potential energy at $t = t_0$. We have found that a counter-gradient heat flux also develops at small scales, but from $\simeq 0.5T_{BV}$, as in LVA's and YW's laboratory experiments (see also Gerz &

Schumann 1991). Thus, the dynamical importance of the counter-gradient heat flux over the first Brunt–Väisälä period may depend upon the Prandtl number but the time of its occurrence is controlled by the initial condition.

5.9.2. *Comparison with the* EDQNM_2 *model*

The heat flux spectrum computed by the EDQNM_2 model is also displayed in figure 18. This spectrum results from a temporal average over the first Brunt–Väisälä period as well. The large-scale behaviour, up to the wavenumber where the spectrum vanishes ($k \simeq 20$) is remarkably well predicted by the EDQNM_2 model. In particular, the maximal amplitude is correct and both spectra vanish at the same wavenumber. The EDQNM_2 spectrum also displays a counter-gradient part, at small scales, so characteristic of the earlier behaviour of the flow. However, the largest absolute value of the counter-gradient region is almost eight times smaller than its DNS counterpart. The insufficiency of the viscous damping in the DNS cannot fully account for this discrepancy and the inability of the EDQNM_2 model to decorrelate the vertical velocity from the temperature fluctuation, as already seen, is very likely responsible for this behaviour.

6. Confinement effects

If kinetic energy is injected at a larger scale than in the calculations presented in this paper, the size of the computational domain being unchanged, the Reynolds number based upon the Taylor microscale increases. The advantage is that viscous effects have less influence upon the flow dynamics; the effect of nonlinearity and buoyancy can thus be better estimated. The drawback is that the largest scales of the flow become affected sooner by the finite size of the computational domain. The consequences of such a confinement upon the flow dynamics are now addressed.

The maximum wavenumber of the kinetic energy spectrum initiating the stratified calculations can be identified with the mesh size M of the grid used in laboratory experiments. Of course, M has to be compared with the size of the computational domain in the DNS and with the size of the tank in laboratory experiments. In the latter case, only the ratio of M to the lateral extent is of relevance since fluid motions are transported at a constant velocity along the channel and are physically confined by the restoring force along the vertical direction. This ratio is equal to 11.3 for the largest mesh size in the experiments of LVA and to 36 in those of YW (in which a single mesh size is used). In the calculations presented in the previous section, this ratio is equal to 9 at $t = t_0$ and we found that no confinement effect exists up to 6 Brunt–Väisälä periods, for $N = \pi$, when temporal evolution of energy components are considered (see the end of § 5.7).

To investigate how confinement modifies the flow dynamics, we have carried out a DNS analogous to run R2 except for the domain side, which was reduced by a factor 2 (run c2 in table 1; note that the isotropic pre-simulation is also different). Since the total energy is contributed by the largest scales, this quantity is most sensitive to a confinement effect. The total energy of run R2 and run c2 are superposed in figure 19. The curves depart very soon, from $0.5T_{BV}$ and the relative difference reaches 20% at $6T_{BV}$. To investigate the origin of this difference, the energy of the vortex and wave parts is displayed in figure 20 for run c2 (and in figure 15*a* for run R2). Two striking differences appear. First, in the confined DNS c2, the vortex part decays at the same rate as the wave energy while, as already seen, this decay rate must be lower. The mean level of the wave energy is the same in runs R2 and c2, however. Thus, the

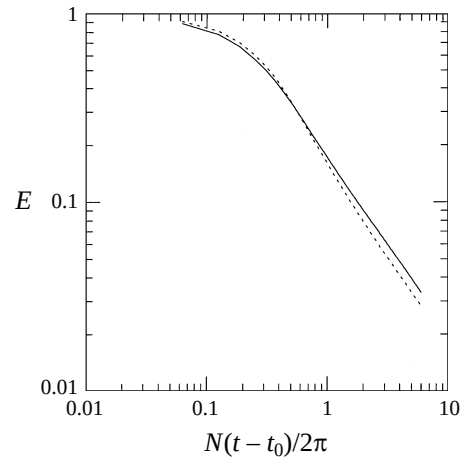

FIGURE 19. DNS results. Total energy (kinetic+potential) as a function of non-dimensional time t/T_{BV}: ——, run R2; - - - -, run c2.

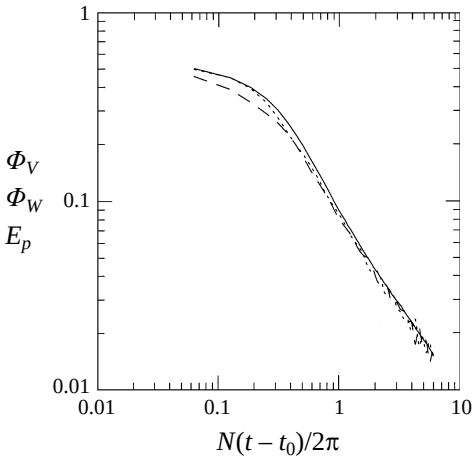

FIGURE 20. DNS results. Energy in the Craya–Herring modes for run c2.: ——, vortex kinetic energy Φ_V; - - - -, wave kinetic energy Φ_W; – – – –, potential energy E_p.

discrepancy in the vortex behaviour accounts for the discrepancy in the total energy observed in figure 19. Secondly, from about $2T_{BV}$, the amplitude of the oscillations in the wave kinetic and potential energies is higher in the confined DNS than in run R2 (this leads to an amplitude of the normalized heat flux four times higher). As shown by van Haren (1993), this effect has to be attributed to the misresolution of the largest scales of the flow in run c2 as time elapses.

7. Discussion and conclusions

The purpose of this paper is to perform a careful comparison between a two-point closure statistical anisotropic model of the EDQNM type (EDQNM$_2$ model) and high-resolution 256^3 direct numerical simulations (DNS), for homogeneous turbulence subjected to a stable stratification. This EDQNM$_2$ model departs from previous attempts (e.g. Holloway 1979; Carnevale & Frederiksen 1983; Sanderson *et*

al. 1991) by dealing with axisymmetric spectra about the vertical direction and by the anisotropy being taken into account both in the closure assumption and in the spectra (the latter depending upon both the modulus of the wavevector and its angle with the vertical direction). The ability of the closure assumption to correctly reproduce the flow dynamics described by the DNS is evaluated by choosing a specific initial condition: the potential energy is half the kinetic energy, the fluctuating temperature field being isotropically distributed and the velocity field being (approximately) that of a homogeneous isotropic turbulence. This initial condition leads to a very small (less than 3 %) correlation between the temperature fluctuation and the vertical velocity throughout the calculations. The flow dynamics are thus mainly driven by nonlinear interactions, at least during the first Brunt–Väisälä period or so, and therefore, are very sensitive to the closure assumption. Calculations have been conducted over 6 Brunt–Väisälä periods.

A remarkable agreement between $EDQNM_2$ predictions and DNS is found in general. One exception concerns the 'vortex' kinetic energy of the flow, which is associated with non-divergent horizontal motions (this vortex part mostly contributes to the horizontal kinetic energy). However, the relative difference between the DNS result and $EDQNM_2$ prediction reaches 14 % only after 6 Brunt–Väisälä periods, the $EDQNM_2$ model overpredicting the vortex kinetic energy. We have checked that this discrepancy is not due to any confinement effect in the DNS. We have found that when energy is injected at a scale greater than or equal to one-fifth of the side of the computational domain a confinement effect appears, that modifies the dynamics of the largest scales of the flow and, thus, of the vortex mode. Another discrepancy between $EDQNM_2$ predictions and DNS results is related to the normalized heat flux: insufficient decorrelation between the vertical velocity and the temperature fluctuations is observed in the $EDQNM_2$ model. The normalized heat flux being only a few percent however, this inadequacy of the model has no dynamical implication.

The comparison between $EDQNM_2$ predictions and DNS results was performed throughout a detailed analysis of the flow dynamics. This analysis was closely connected with the experimental works by Lienhardt & Van Atta (1990) and Yoon & Warhaft (1990), respectively referred to as LVA and YW in the text. We have found that the flow dynamics are controlled by potential energy being transferred from large to small scales at a higher rate than kinetic energy, during the first Brunt–Väisälä period. This behaviour is well-known to hold also for a passive scalar (e.g. Lesieur 1990) and was observed in stably stratified flows by Holloway & Ramsden (1988). In our calculations, this behaviour has important consequences: the total energy decays at a higher rate than its isotropic counterpart during the first Brunt–Väisälä period. Also, vertical kinetic energy appears to be converted into potential energy at the very beginning of the calculation, to make up for the irreversible transfer of potential energy toward small scales. This conversion of vertical kinetic energy into potential energy, despite the fact that there is more potential energy than vertical kinetic energy at $t = t_0$, yields analogies with laboratory experiments, in which there is very little potential energy behind the grid. Thus, in LVA's experiment, 60% of the vertical kinetic energy is used to create potential energy, against 30% in our calculations. This factor 2 only indicates how important to the flow dynamics is the high rate of potential energy transfers. Also, we find that the vertical kinetic energy displays a similarity law as in LVA's experiment, with the same shape but different level. Another consequence is that the potential energy transferred at small scales drives a counter-gradient heat flux at those scales, that occurs from the beginning of the calculation and persists throughout the calculations. This flux appears however to

play no dynamical role on the smallest scales during the first Brunt–Väisälä period. The same result is observed in LVA's experiments, in which the counter-gradient heat flux at small scales is insignificant. The existence of a persistent counter-gradient heat flux at small scales has already been noted by several authors, in numerical and laboratory experiments on stratified turbulence (Gerz & Schumann 1996; Komori & Nagata 1996), as well as in two- and three-dimensional numerical experiments on breaking gravity waves (Holloway & Ramsden 1988; Bouruet-Aubertot, Sommeria & Staquet 1996).

It is noteworthy that the horizontal kinetic energy remains nearly unaffected, over $0.7T_{BV}$, by the processes just described. That the horizontal kinetic energy exhibits such an independent behaviour was also observed by LVA, YW and Komori & Nagata (1996) in their wind-tunnel laboratory experiments.

Our calculations simulate a longer evolution of the flow dynamics than laboratory experiments, in which the flow develops for at most one Brunt–Väisälä period. We find that the flow dynamics are marked by a second event at about $1.5T_{BV}$. At large scales, the heat flux collapses; also, the ratio L_b/L_T (proportional to the square root of the vertical kinetic energy over the potential energy) reaches a constant value (equal to $2/3$); as well, large-scale energetic horizontal motions, forming the vortex part of the flow, emerge from turbulence. At smaller scales, the vertical kinetic energy and, especially, the dissipation rate of kinetic energy display a similarity law for different values of N and ν. This law indicates that these quantities are controlled by buoyancy effects. We thus find that the heat flux collapses at the same time that the dissipative, and thus smallest, scales of the flow are dominated by buoyancy forces. One explanation is that the collapse of the largest scales, in insufficiently feeding the smallest scales with energy, makes them sensitive to the buoyancy force. In other words, these smallest scales become anisotropic from $1.5T_{BV}$. LVA found that the smallest scales remain nearly unaffected by buoyancy forces over the whole duration of the flow ($\simeq 0.8T_{BV}$ at most), which is consistent with our results.

A remarkable point of our study is that only one quantity behaves identically in our DNS, in the EDQNM_2 model and in LVA's and YW's experiments. This is the ratio of the dissipation rate of kinetic energy to the heat flux. This ratio quantifies the instantaneous mixing efficiency and oscillates identically, below the maximum value of $\simeq 0.2$, in all fours sets of data. Thus, this quantity seems to be independent of initial conditions.

The organization of a stably stratified flow into quasi-horizontal motions, besides a field of internal waves, is a common feature of stably stratified flows (e.g. Lin & Pao 1974; Riley *et al.* 1981; Herring & Métais 1989; Fincham *et al.* 1996). We have found that the energetic dominance of these motions is the more pronounced the larger N and the viscosity ν. The existence of a two-dimensional dynamics for such motions was investigated by Herring & Métais (1989) for forced stably stratified turbulence, through the search for an inverse cascade. A degree of inverse cascade to large scales was found but with no $k^{-5/3}$ range. Numerical and physical arguments are provided by those authors to account for these results.

Our work offers interesting perspectives. While an increase of the resolution by only a factor 2 in the DNS is nearly inaccessible, the maximum wavenumber in the EDQNM_2 model can be multiplied by a factor 10 and the code still be run. The good validation of the EDQNM_2 model demonstrated in this paper, at least for the wave part of the flow, thus permits us to envisage with confidence calculations at higher Reynolds numbers, even higher than those of laboratory experiments. The investigation of the smallest-scale motions, which are mostly contributed by the wave

part of the flow, would be of great interest. How does their anisotropic behaviour depend upon the Reynolds number? An answer to this question would have important implications for the subgrid-scale modelling of stably-stratified flows.

Another important implication of high-Reynolds-number studies, affordable with the EDQNM$_2$ model, is related to energy spectra. In geophysical flows, measurements of velocity and especially temperature fluctuations at small scales (not affected by Earth's rotation) collapse to a unique form ($\alpha N^2 k_z^3$) when their variance spectrum is plotted as a function of the vertical wavenumber k_z (e.g. Gregg 1989, for the ocean; Hostetler & Gardner 1994, for the stratosphere). No such spectra are obtained in our calculations. In geophysical flows, these spectra are most often interpreted as resulting from internal gravity wave breaking and recent direct (two-dimensional) numerical simulations of breaking gravity waves by Bouruet-Aubertot *et al.* (1996) were able to reproduce them. In the simulations performed by those authors, the turbulent regime results from mostly resonant and, next, mostly non-resonant interactions among waves, that lead to localized breaking as soon as the local Froude number exceeds a value of order 1. The reason why our data do not collapse on such spectra may be due to the low value reached by the Reynolds number at the time interacting internal waves have set up at the largest scales. A high-Reynolds-number EDQNM$_2$ calculation would thus be extremely valuable to investigate this point. Also, it would be desirable that experimental energy spectra as a function of the vertical wavenumber be available to complement this discussion.

This work benefited from discussions with Claude Cambon. Calculations have been performed on the Cray C98 of IDRIS (CNRS computer center), thanks to computing time allocated by the Scientific Council of IDRIS. We thank Gilles Grasseau from IDRIS, for his help in improving the performance of the code.

Appendix. Full energy transfer terms for the EDQNM$_1$ and EDQNM$_2$ models

The fully nonlinear transfer terms for the EDQNM$_1$ and EDQNM$_2$ models discussed in the paper are given in this Appendix, as can be found in Godeferd (1994). The easiest and soundest way of numerically time solving the system of equations (21)–(24) is to use the sum and difference of the wave and potential energy variables, as proposed in § 4.1.2. The energy transfer terms for these variables are therefore

$$\mathscr{T}^2(\boldsymbol{k}) + \mathscr{T}^3(\boldsymbol{k}) = \mathrm{Re}\left(\mathscr{T}^{Z_1}(\boldsymbol{k}) + \mathscr{T}^{Z_2}(\boldsymbol{k})\right), \tag{A 1}$$

$$\mathscr{T}^2(\boldsymbol{k}) - \mathscr{T}^3(\boldsymbol{k}) + I\mathscr{T}^{\Psi}(\boldsymbol{k}) = -\mathscr{T}^{Z_1}(\boldsymbol{k}) + \mathscr{T}^{Z_2}(\boldsymbol{k}), \tag{A 2}$$

where the $\mathscr{T}^{Z_1}$ and $\mathscr{T}^{Z_2}$ parts are given below, as well as the $\mathscr{T}^1$ transfer term. Re denotes the real part.

$$\begin{aligned}
\mathscr{T}^1(\boldsymbol{k}) = \sum_{\{\varepsilon,\varepsilon',\varepsilon''\}\in\{0,\pm1\}^3} & \frac{-1}{(|\varepsilon|+1)(|\varepsilon'|+1|)(|\varepsilon''|+1)} \int_{\boldsymbol{k}+\boldsymbol{p}+\boldsymbol{q}=0} \frac{\tau_{kpq}^{\varepsilon\varepsilon'\varepsilon''}}{4} \\
& \times \left[(\boldsymbol{k}\cdot\boldsymbol{e}^{|\varepsilon'|+1}(\boldsymbol{p}))(\boldsymbol{e}^1(\boldsymbol{k})\cdot\boldsymbol{e}^{|\varepsilon''|+1}(\boldsymbol{q})) + (\boldsymbol{k}\cdot\boldsymbol{e}^{|\varepsilon''|+1}(\boldsymbol{q}))(\boldsymbol{e}^1(\boldsymbol{k})\cdot\boldsymbol{e}^{|\varepsilon'|+1}(\boldsymbol{p}))\right] \\
& \times (\boldsymbol{e}^{|\varepsilon|+1}(\boldsymbol{k})\cdot\boldsymbol{e}^1(\boldsymbol{k})) \\
& \times \left\{\left[(\boldsymbol{p}\cdot\boldsymbol{e}^{|\varepsilon|+1}(\boldsymbol{k}))(\boldsymbol{e}^{|\varepsilon'|+1}(\boldsymbol{p})\cdot\boldsymbol{e}^{|\varepsilon''|+1}(\boldsymbol{q})) - (\boldsymbol{k}\cdot\boldsymbol{e}^{|\varepsilon''|+1}(\boldsymbol{q}))(\boldsymbol{e}^{|\varepsilon|+1}(\boldsymbol{k})\cdot\boldsymbol{e}^{|\varepsilon'|+1}(\boldsymbol{p}))\right]\right. \\
& \times (\Phi^{|\varepsilon'|+1}(\boldsymbol{p}) + I\varepsilon'\Psi(\boldsymbol{p}) - \Phi^{|\varepsilon|+1}(\boldsymbol{k}) - I\varepsilon\Psi(\boldsymbol{k}))(\Phi^{|\varepsilon''|+1}(\boldsymbol{q}) + I\varepsilon''\Psi(\boldsymbol{q}))
\end{aligned}$$

$$+\Big[\varepsilon\varepsilon'(\boldsymbol{k}\cdot\boldsymbol{e}^{|\varepsilon''|+1}(\boldsymbol{q}))(\Phi^3(\boldsymbol{p})-I\varepsilon'\Psi(\boldsymbol{p})-\Phi^3(\boldsymbol{k})+I\varepsilon\Psi(\boldsymbol{k}))$$
$$\times(\Phi^{|\varepsilon''|+1}(\boldsymbol{q})+I\varepsilon''\Psi(\boldsymbol{q}))+\varepsilon\varepsilon''(\boldsymbol{q}\cdot\boldsymbol{e}^{|\varepsilon|+1}(\boldsymbol{k}))(\Phi^3(\boldsymbol{p})$$
$$-I\varepsilon'\Psi(\boldsymbol{p}))(\Phi^{|\varepsilon|+1}(\boldsymbol{k})+I\varepsilon\Psi(\boldsymbol{k}))\Big]\Big\}\,\mathrm{d}^3\boldsymbol{p}, \tag{A 3}$$

$$\mathscr{T}^{Z_1}(\boldsymbol{k})=\sum_{\{\varepsilon,\varepsilon',\varepsilon''\}\in\{0,\pm1\}^3}\frac{-1}{(|\varepsilon|+1)(|\varepsilon'|+1|)(|\varepsilon''|+1)}\int_{\boldsymbol{k}+\boldsymbol{p}+\boldsymbol{q}=0}\frac{\tau_{kpq}^{\varepsilon\varepsilon'\varepsilon''}}{4}$$
$$\times\Big[(\boldsymbol{k}\cdot\boldsymbol{e}^{|\varepsilon'|+1}(\boldsymbol{p}))(\boldsymbol{e}^2(\boldsymbol{k})\cdot\boldsymbol{e}^{|\varepsilon''|+1}(\boldsymbol{q}))+(\boldsymbol{k}\cdot\boldsymbol{e}^{|\varepsilon''|+1}(\boldsymbol{q}))(\boldsymbol{e}^2(\boldsymbol{k})\cdot\boldsymbol{e}^{|\varepsilon'|+1}(\boldsymbol{p}))\Big]$$
$$\times(\boldsymbol{e}^{|\varepsilon|+1}(\boldsymbol{k})\cdot\boldsymbol{e}^2(\boldsymbol{k})+\varepsilon)$$
$$\times\Big\{\Big[(\boldsymbol{p}\cdot\boldsymbol{e}^{|\varepsilon|+1}(\boldsymbol{k}))(\boldsymbol{e}^{|\varepsilon'|+1}(\boldsymbol{p})\cdot\boldsymbol{e}^{|\varepsilon''|+1}(\boldsymbol{q}))-(\boldsymbol{k}\cdot\boldsymbol{e}^{|\varepsilon''|+1}(\boldsymbol{q}))(\boldsymbol{e}^{|\varepsilon|+1}(\boldsymbol{k})\cdot\boldsymbol{e}^{|\varepsilon'|+1}(\boldsymbol{p}))\Big]$$
$$\times(\Phi^{|\varepsilon'|+1}(\boldsymbol{p})+I\varepsilon'\Psi(\boldsymbol{p})-\Phi^{|\varepsilon|+1}(\boldsymbol{k})-I\varepsilon\Psi(\boldsymbol{k}))(\Phi^{|\varepsilon''|+1}(\boldsymbol{q})+I\varepsilon''\Psi(\boldsymbol{q}))$$
$$+\Big[\varepsilon\varepsilon'(\boldsymbol{k}\cdot\boldsymbol{e}^{|\varepsilon''|+1}(\boldsymbol{q}))(\Phi^3(\boldsymbol{p})-I\varepsilon'\Psi(\boldsymbol{p})-\Phi^3(\boldsymbol{k})+I\varepsilon\Psi(\boldsymbol{k}))(\Phi^{|\varepsilon''|+1}(\boldsymbol{q})+I\varepsilon''\Psi(\boldsymbol{q}))$$
$$+\varepsilon\varepsilon''(\boldsymbol{q}\cdot\boldsymbol{e}^{|\varepsilon|+1}(\boldsymbol{k}))(\Phi^3(\boldsymbol{p})-I\varepsilon'\Psi(\boldsymbol{p}))(\Phi^{|\varepsilon|+1}(\boldsymbol{k})+I\varepsilon\Psi(\boldsymbol{k}))\Big]\Big\}\,\mathrm{d}^3\boldsymbol{p}, \tag{A 4}$$

$$\mathscr{T}^{Z_2}(\boldsymbol{k})=\sum_{\{\varepsilon,\varepsilon',\varepsilon''\}\in\{0,\pm1\}^3}\frac{-1}{(|\varepsilon|+1)(|\varepsilon'|+1|)(|\varepsilon''|+1)}\int_{\boldsymbol{k}+\boldsymbol{p}+\boldsymbol{q}=0}\frac{\tau_{kpq}^{\varepsilon\varepsilon'\varepsilon''}}{4}$$
$$\times\Big[\varepsilon'(\boldsymbol{k}\cdot\boldsymbol{e}^{|\varepsilon''|+1}(\boldsymbol{q}))+\varepsilon''(\boldsymbol{k}\cdot\boldsymbol{e}^{|\varepsilon'|+1}(\boldsymbol{p}))\Big](\boldsymbol{e}^{|\varepsilon|+1}(\boldsymbol{k})\cdot\boldsymbol{e}^2(\boldsymbol{k})+\varepsilon)$$
$$\times\Big\{\Big[(\boldsymbol{p}\cdot\boldsymbol{e}^{|\varepsilon|+1}(\boldsymbol{k}))(\boldsymbol{e}^{|\varepsilon'|+1}(\boldsymbol{p})\cdot\boldsymbol{e}^{|\varepsilon''|+1}(\boldsymbol{q}))-(\boldsymbol{k}\cdot\boldsymbol{e}^{|\varepsilon''|+1}(\boldsymbol{q}))(\boldsymbol{e}^{|\varepsilon|+1}(\boldsymbol{k})\cdot\boldsymbol{e}^{|\varepsilon'|+1}(\boldsymbol{p}))\Big]$$
$$\times(\Phi^{|\varepsilon'|+1}(\boldsymbol{p})+I\varepsilon'\Psi(\boldsymbol{p})-\Phi^{|\varepsilon|+1}(\boldsymbol{k})-I\varepsilon\Psi(\boldsymbol{k}))(\Phi^{|\varepsilon''|+1}(\boldsymbol{q})+I\varepsilon''\Psi(\boldsymbol{q}))$$
$$+\Big[\varepsilon\varepsilon'(\boldsymbol{k}\cdot\boldsymbol{e}^{|\varepsilon''|+1}(\boldsymbol{q}))(\Phi^3(\boldsymbol{p})-I\varepsilon'\Psi(\boldsymbol{p})-\Phi^3(\boldsymbol{k})+I\varepsilon\Psi(\boldsymbol{k}))$$
$$\times(\Phi^{|\varepsilon''|+1}(\boldsymbol{q})+I\varepsilon''\Psi(\boldsymbol{q}))+\varepsilon\varepsilon''(\boldsymbol{q}\cdot\boldsymbol{e}^{|\varepsilon|+1}(\boldsymbol{k}))(\Phi^3(\boldsymbol{p})$$
$$-I\varepsilon'\Psi(\boldsymbol{p}))(\Phi^{|\varepsilon|+1}(\boldsymbol{k})+I\varepsilon\Psi(\boldsymbol{k}))\Big]\Big\}\,\mathrm{d}^3\boldsymbol{p}. \tag{A 5}$$

The vectors $\boldsymbol{e}^i$ are defined in (5), and the damping associated with each of the eight triadic interactions is

$$\tau_{kpq}^{\varepsilon\varepsilon'\varepsilon''}=\left[(\tau_{kpq})^{-1}-\mathrm{i}N(\varepsilon\sin\theta_k+\varepsilon''\sin\theta_p+\varepsilon''\sin\theta_q)\right]^{-1}\ . \tag{A 6}$$

In equations (A 3), (A 4) and (A 5), we can identify products of double correlation spectra, denoting the fact that a quasi-Gaussian assumption has been used for replacing the third-order correlations. Also, one sees that dot products of the unit vectors of the local frame appear, these products being related to the geometry of the triangles $\boldsymbol{k}$, $\boldsymbol{p}$, $\boldsymbol{q}$ over which the integrals are computed.

If N is set to zero in (A 6), the closure assumption of the isotropic EDQNM model is recovered. Using (A 6) with $N=0$ in the EDQNM$_2$ model yields the simplified EDQNM$_1$ model. If, moreover, $N=0$ in the left-hand sides of equations (21)–(24) also, then the isotropic EDQNM model is recovered.

REFERENCES

André, J. C. & Lesieur, M. 1977 Influence of helicity on high Reynolds number isotropic turbulence. *J. Fluid Mech.* **81**, 187–207.

Bouruet-Aubertot, P., Sommeria, J. & Staquet, C. 1996 Stratified turbulence produced by internal wave breaking: two-dimensional numerical experiments. *Dyn. Atmos. Oceans* **23**, 357–369.

Cambon, C. 1989 Spectral approach to axisymmetric turbulence in a stratified fluid. *Advances in Turbulence* 2. Springer.

Cambon, C. & Godeferd, F. S. 1993 Inertial transfers in freely decaying, rotating, stably stratified and MHD turbulence. *AIAA Progress in Astronautics and Aeronautics Series* (ed. H. Branover & Y. Unger), vol. 162, pp. 150–168.

Canuto, C., Hussaini, M. Y., Quarteroni, A. & Zang, T. A. 1988 *Spectral Methods in Fluid Dynamics*. Springer.

Carnevale, G. F. & Frederiksen, J. S. 1983 A statistical dynamical theory of strongly nonlinear internal gravity waves. *Geophys. Astrophys. Fluid Dyn.* **23**, 175–207.

Chasnov, J. R. 1996 Some similarity states of stably stratified homogeneous turbulence. *Dyn. Atmos. Oceans* **23**, 183–192.

Craya, A. 1958 Contribution à l'analyse de la turbulence associée à des vitesses moyennes. *Tech. Rep.* 345 Ministère de l'Air.

Daubner, S. & Zeitlin, V. 1996 On the stationary energy spectra for unidirectionally propagating internal waves. *Phys. Lett.* A **214**, 33–39.

Fincham, A. M., Maxworthy, T. & Spedding, G. R. 1996 Energy dissipation and vortex structure in freely-decaying stratified grid-turbulence. *Dyn. Atmos. Oceans* **23**, 155–169.

Gerz, T. & Schumann, U. 1991 Direct simulation of homogeneous turbulence and gravity waves in sheared und unsheared stratified flows. *Turbulent Shear Flows 7*, pp. 27–45. Springer.

Gerz, T. & Schumann, U. 1996 A possible explanation of countergradient fluxes in homogeneous turbulence. *Theor. Comput. Fluid Dyn.* **8**, 169–181.

Gerz, T. & Yamazaki, H. 1993 Direct numerical simulation of buoyancy-driven turbulence in stably stratified fluid. *J. Fluid Mech.* **249**, 415–440.

Godeferd, F. S. 1994 Introduction d'une partition ondes-turbulence dans les modèles de transport pour les écoulements turbulents stablement stratifiés. PhD thesis, École Centrale de Lyon.

Godeferd, F. S. & Cambon, C. 1994 Detailed investigation of energy transfers in homogeneous stratified turbulence. *Phys. Fluids* **6**, 2084–2100.

Godeferd, F. S. & Staquet, C. 1998 Statistical modelling and direct numerical simulations of decaying stably-stratified turbulence: Large and small scales anisotropy. *J. Fluid Mech.*, in preparation.

Gregg, M. 1989 Diapycnal mixing in the thermocline: a review. *J. Geophys. Res.* **92**, 5249–5286.

Hanazaki, H. & Hunt, J. C. R. 1996 Linear processes in unsteady stably stratified turbulence. *J. Fluid Mech.* **318**, 303–337.

Haren, L. van 1993 Étude théorique et modélisation de la turbulence en présence d'ondes internes. PhD thesis, École Centrale de Lyon.

Haren, L. van, Staquet, C. & Cambon, C. 1996 Decaying stratified turbulence: comparison between a two-point closure EDQNM model and direct numerical simulations. *Dyn. Atmos. Oceans* **23**, 217–233.

Hart, R. W. 1981 Generalized scalar potentials for linearized three-dimensional flows with vorticity. *J. Fluid Mech.* **24**, 1418–1420.

Herr, S., Wang, L.-P. & Collins, L. R. 1996 EDQNM model for a passive scalar with a uniform mean gradient. *Phys. Fluids* **8**, 1588–1608.

Herring, J. R. 1974 Approach of axisymmetric turbulence to isotropy. *Phys. Fluids* **17**, 859–872.

Herring, J. R. & Kraichnan, R. H. 1971 *Comparison of some Approximations for Isotropic Turbulence, Statistical Models and Turbulence*. Lecture notes in Physics, vol. 12. Springer-Verlag.

Herring, J. R. & Metais, O. 1989 Numerical experiments in forced stably stratified turbulence. *J. Fluid Mech.* **202**, 97–115.

Holliday, D. & McIntyre, M. E. 1981 On potential energy density in an incompressible stratified fluid. *J. Fluid Mech.* **107**, 221–225.

Holloway, G. 1979 On the spectral evolution of strongly interacting waves. *Geophys. Astrophys. Fluid Dyn.* **11**, 271–287.

Holloway, G. 1988 The buoyancy flux from internal gravity wave breaking. *Dyn. Atmos. Oceans* **12**, 107–125.

Holloway, G. & Hendershot, M. C. 1977 Statistical closure for nonlinear Rossby waves. *J. Fluid Mech.* **82**, 747–765.

Holloway, G. & Ramsden, D. 1988 Theories of internal wave interaction and stably stratified turbulence: testing against direct numerical experimentation. In *Small-Scale Turbulence and Mixing in the Ocean*, pp. 363–378. Elsevier.

Hopfinger, E. J. 1987 Turbulence in stratified fluids: a review. *J. Geophys. Res.* **92**, 5287–5303.

Hostetler, C. A. & Gardner, C. S. 1994 Observations of horizontal and vertical wave number spectra of gravity wave motions in the stratosphere and mesosphere over the mid-Pacific. *J. Geophys. Res.* **99**, 1283–1302.

Itsweire, E. C., Helland, K. N. & Van Atta, C. W. 1986 The evolution of grid-generated tubulence in a stably stratified fluid. *J. Fluid Mech.* **162**, 299–338.

Kimura, Y. & Herring, J. R. 1996 Diffusion in stably stratified turbulence. *J. Fluid Mech.* **328**, 253–269.

Komori, S. & Nagata, K. 1996 Effects of molecular diffusivities on counter-gradient scalar and momentum transfer in strongly stable stratification. *J. Fluid Mech.* **326**, 205–237.

Lelong, M. P. & Riley, J. J. 1991 Internal wave-vortical mode interactions in strongly stratified flows. *J. Fluid Mech.* **232**, 1–19.

Lesieur, M. 1990 *Turbulence in Fluids,* 2nd edn. Kluwer.

Lienhard, J. H. & Van Atta, C. W. 1990 The decay of turbulence in thermally stratified flow. *J. Fluid Mech.* **210**, 57–112 (referred to herein as LVA).

Lin, J.-T. & Pao, Y.-H. 1979 Wakes in stratified fluids. *Ann. Rev. Fluid Mech.* **11**, 317–338.

Metais, O. & Herring, J. R. 1989 Numerical simulations of freely evolving turbulence in stably stratified fluids. *J. Fluid Mech.* **202**, 117–148.

Metais, O. & Lesieur, M. 1992 Spectral large-eddy simulation of isotropic and stably stratified turbulence. *J. Fluid Mech.* **239**, 157–194.

Muller, P., Holloway, G., Henyey, F. & Pomphrey, N. 1986 Nonlinear interactions among internal gravity waves. *Rev. Geophys.* **24**, 493–536.

Orszag, S. A. 1970 Analytical theories of turbulence. *J. Fluid Mech.* **41**, 363–386.

Orszag, S. A. 1977 Statistical theory of turbulence. *Fluid Dynamics 1973, Les Houches Summer School of Theoretical Physics* (ed. R. Balian & J. L. Peube), pp. 237–374. Gordon and Breach.

Orszag, S. A. & Patterson, G. S. 1972 Numerical simulation of three-dimensional homogeneous isotropic turbulence. *Phys. Rev. Lett.* **28**, 76–79.

Phillips, O. M. 1977 *The Dynamics of the Upper Ocean*, 2nd edn Cambridge University Press.

Ramsden, D. & Holloway, G. 1992 Energy transfers across an internal wave-vortical mode spectrum. *J. Geophys Res.* **97**, 3659–3668.

Riley, J. J., Metcalfe, R. W. & Weissman, M. A. 1981 Direct numerical simulations of homogeneous turbulence in density-stratified fluids. In *Proc. AIP Conf. on Nonlinear Properties of Internal Waves* (ed. J. B. West), pp. 79–112. American Institute of Physics.

Sanderson, R. C., Hill, J. C. & Herring, J. R. 1986 Transient behavior of a stably stratified homogeneous turbulent flow. In *Advances in Turbulence* (ed. G. Comte-Bellot & J. Mathieu), pp. 184–190. Springer.

Sanderson, R. C., Leonard, A. D., Herring, J. R. & Hill, J. C. 1991 Fossil and active turbulence. In *Turbulence and Coherent Structures* (ed. O. Metais & M. Lesieur), pp. 429–448. Springer.

Schatzman, E. 1993 Transport of angular momentum and diffusion by the action of internal waves. *Astron. Astrophys.* **279**, 431.

Schatzman, E. 1996 Diffusion process produced by random internal waves. *J. Fluid Mech.* **322**, 355–382.

Sidi, C. 1995 Some observed properties of small scales ($o[1..10^2\,m]$) fluctuations in the stratosphere. *Proc. Euromech Colloquium 339, Lyon, Sept. 6–9.*

Spedding, G. R., Browand, F. K. & Fincham, A. M. 1996 Turbulence, similarity scaling and vortex geometry in the wake of a towed sphere in a stably stratified fluid. *J. Fluid Mech.* **314**, 53–103.

Staquet, C. & Riley, J. J. 1989 On the velocity field associated with potential vorticity. *Dyn. Atmos. Oceans* **14**, 93–123.

Thoroddsen, S. T. & Van Atta, C. W. 1992 The influence of stable stratification on small-scale anisotropy and dissipation in turbulence. *J. Geophys. Res.* **97**, 3647–3658.

Thoroddsen, S. T. & Van Atta, C. W. 1996 The influence of stable stratification on small-scale anisotropy and dissipation in turbulence. *J. Fluid. Mech.* **322**, 383–409.

Yoon, K. & Warhaft, Z. 1990 The evolution of grid-generated turbulence under conditions of stable thermal stratification. *J. Fluid Mech.* **215**, 601–638 (referred to herein as YW).

Zakharov, V. E., L'vov, V. S. & Falkovich, G. 1992 *Kolmogoroff Spectra of Turbulence I. Wave Turbulence*. Springer.